Chapter 4

Rainfall Distribution in Landfalling Tropical Cyclones

Zifeng Yu and Yuqing Wang

Additional information is available at the end of the chapter

http://dx.doi.org/10.5772/intechopen.75910

Abstract

Accurate prediction of rainfall distribution in landfalling tropical cyclones (LTCs) is very important to disaster prevention but quite challenging to operational forecasters. This chapter will describe the rainfall distribution in LTCs, including both axisymmetric and asymmetric distributions and their major controlling parameters, such as environmental vertical wind shear, TC intensity and motion, and coastline. In addition to the composite results from many LTC cases, several case studies are also given to illustrate the predominant factors that are key to the asymmetric rainfall distribution in LTCs. Future directions in this area and potential ways to improve the operational forecasts of rainfall distribution in LTCs are also discussed briefly.

Keywords: tropical cyclones, landfalling, rainfall distribution, vertical wind shear, typhoon, precipitation, intensity

1. Introduction

Landfalling tropical cyclones (LTCs) often bring very heavy rainfall to the affected regions so that many extreme rainfall events are related to LTCs around the world. Heavy rainfall associated with LTCs is one of the most devastating natural disasters in the coastal regions in the world, which could bring unexpected flash floods and landslides to inflict huge losses in properties and human lives. Examples of some record-breaking heavy rainfall events induced by LTCs include 24-h rainfall of 1062 mm at Linzhuang in Henan Province of Mainland China caused by landfalling Typhoon Nina (7503) in 1975 and 24-h rainfall of about 1300 mm in southern Taiwan caused by Typhoon Morakot in 2009. Therefore, the rainfall distribution in a LTC is of particular importance to meteorologists and disaster preventions.

However, though tropical cyclone (TC) track forecasts have achieved great improvements in the past decades [1, 2], improvements in TC rainfall forecasts have been largely behind. Even when the TC track is well predicted, the rainfall distribution and intensity are often poorly predicted, especially for rainfall distribution and storm structure. Therefore, understanding the characteristics and the factors that control rainfall distribution in LTCs is very important for improving real-time operational rainfall forecasts.

Distribution of rainfall in LTCs may be affected by many processes and factors, such as TC motion, intensity, landfalling location and time, large-scale environmental conditions, terrains in the coastal region, and so on. Previous studies have shown that rainfall in a TC can be largely modulated by the environmental vertical wind shear (VWS) [3–12], the planetary vorticity gradient [13–16], the storm motion [16, 17], the friction-induced asymmetric boundary layer convergence in a moving TC [18], the asymmetric environmental moisture distribution in [19], and also the convectively coupled vortex-Rossby waves in the eyewall [20–22].

To investigate the rainfall distribution in LTCs and the associated physical process, the rainfall distribution in a LTC is often decomposed into a wavenumber (WN)-0 (or an azimuthal mean) component and a series of higher-WN components in [23–26]. Recently, with the improvements of satellite-retrieved rain data application, some observational studies have focused on the asymmetric TC rainfall distribution and related different physical processes. Rogers et al. [27] suggested that the combination of VWS and storm motion could explain well the rainfall asymmetry in Hurricane Bonnie. Lonfat et al. [23] analyzed the global rainfall distribution in TCs based on the Tropical Rainfall Measuring Mission (TRMM) rain estimates and studied the relationships between the TC rainfall distribution and the TC motion over oceans in the world. It has been shown that the storm motion alone, however, could not fully explain the basin-to-basin variability in the rainfall asymmetry, suggesting that other mechanisms must contribute to the asymmetric rainfall distribution, such as the environmental VWS, which has been investigated extensively (e.g., [14, 24, 28]).

Chen et al. [24] investigated the effects of both VWS and storm motion on TC rainfall asymmetries based on composite analyses using the TRMM rain data. The results showed that the TC rainfall asymmetry generally depends on the juxtaposition and relative magnitude of the environmental VWS and the TC motion over the open ocean. Subsequent composite analyses of the TC rainfall asymmetry related to environmental VWS by using the satellite-based rainfall estimates have further confirmed the relationship between the spatial distribution of TC rainfall and the environmental VWS [29–31]. Namely, the maximum rainfall predominantly occurs in the downshear-left quadrant in a TC that is embedded in an environmental VWS (facing down the shear vector), while the effect of TC translation becomes an important factor for a TC embedded in the relatively low VWS environment. Reasor et al. [32] reconfirmed that the environmental VWS is the primary factor affecting the eyewall convective asymmetry in TCs based on Doppler radar data composite analysis.

Most of previous studies have mainly focused on the rainfall distributions in TCs before landfall or over the open oceans. In addition to the effects of environmental VWS, TC intensity and motion, the rainfall asymmetries in a LTC may also be affected by non-uniform surface characteristics, such as land-sea contrast, coastline, topography, and mesoscale convective activities that resulted from interactions with other synoptic weather systems [33–47].

Some numerical studies have found that the asymmetric structure of a LTC and the associated asymmetric rainfall distribution could be forced by land-sea contrast [20, 48–52]. Based on idealized simulations for LTCs on an *f*-plane, Li et al. [43, 44] showed that rainfall asymmetry became larger after landfall with larger VWS, and land surface roughness would initially affect rainfall distribution in the outer region. Xu et al. [45] indicated that the asymmetric rainfall percentage toward the right quadrant relative to the coastline would have an obvious increase in LTCs, which might be related to the land-sea roughness gradient.

In an early observational study, based on the airborne radar reflectivity data from systems onboard three National Oceanic and Atmospheric Administration (NOAA) aircrafts during 6 days for Hurricane Allen (1980), Marks [3] showed that changes in both the storm intensity and the eyewall radius had little impact on the total rainfall of the storm. However, the axisymmetric rainfall distribution in TCs has received further attention in recent years, with the focus on the relationship between TC intensity and axisymmetric rainfall distribution. Lonfat et al. [23] explored the axisymmetric rainfall distribution in TCs with different intensities during 1998–2000 over global oceans using the TRMM retrieved rain data. They found that the peak radial axisymmetric rain rate increased with increasing TC intensity. More recent studies have confirmed that TC intensity and intensity change are closely related with rainfall and rainfall change over the open ocean [53–57]. However, the relationship of axisymmetric rainfall distribution and TC intensity in LTCs is reported to be more complicated in Yu et al. [26].

This chapter aims to document the evolution of rainfall distribution in LTCs, taking those that made landfall over China as examples, and to systematically examine the effects of various factors, including TC intensity and motion, environmental VWS, and land-sea contrast, on both the axisymmetric and asymmetric rainfall distributions from 24 h prior, to landfall, and to 24 h after landfall. Section 2 introduces the data used and the analysis methods. Sections 3 and 4 present, respectively, the axisymmetric and asymmetric rainfall distributions in LTCs and their relationship with the different factors. Section 5 shows several case studies to demonstrate the complexity of rainfall distribution in LTC. Some remaining issues are discussed in Section 6. Section 7 gives the concluding remarks.

2. Data and methodology

2.1. TRMM 3B42 data

With the development of satellite observing systems, the satellite-retrieved rainfall estimates are more widely applied to both weather and climate research, in particular for the study of rainfall in TCs either over the open oceans or near landfall. Though rain gauge data are routinely available, they are not dense enough or even spare in many important regions, such as over terrains and in the coastal areas over land. Weather radars could give good temporal and spatial resolutions, but they are limited by their area coverage due to unevenly distributed radar sites and inter-radar calibration that could lower the capability and accuracy in rainfall estimation. Therefore, the satellite rainfall estimates are good choices to study rainfall characteristics, especially over the open oceans and coastal and mountainous areas where surface observations are limited.

Many studies have evaluated the performances of TRMM satellite rainfall retrievals in capturing the rainfall features in LTCs [58–62]. These studies have shown that the TRMM 3B42 rain data can provide quite reasonable rainfall distributions in LTCs compared with surface data like gauge and radar observations, although they are generally more accurate over ocean than over land. The rainfall distribution evolution in LTCs during 24 h prior to landfall (t = −24) to 24 h after landfall (t = 24) over China will be discussed in Sections 3 and 4 based on the TRMM 3B42 rain estimates.

2.2. Reanalysis data

The horizontal winds obtained from NCEP/NCAR (National Centers for Environmental Predictions/National Center for Atmospheric Research) global reanalysis data [63] are used to calculate the large-scale environmental VWS, which was defined as the 200-hPa and 850-hPa wind vector differences averaged within a 500-km radius from each TC center at every 6-h interval as in [25, 26].

2.3. Best-track TC data

In total, 133 LTCs over China are included in the results discussed in the following sections (**Table 1**), with the lowest intensity of tropical storm (CAT2) from 24 h before landfall (t = −24), to landfall time (t = 0), and to 24 h after landfall (t = 24). Among them, 24, 39, 32, 29, and 9 LTCs, respectively, made a landfall in Hainan (HN), Guangdong (GD), Taiwan (TW), Fujian (FJ), and Zhejiang (ZJ) provinces in China (**Figure 1a–e**). The coastline directions of the five regions are also shown in **Figure 1f**, namely, 45, 16, 76, 53, and 45° from the east, respectively, in HN, GD, TW, FJ, and ZJ.

The best-track TC data are those products from the Shanghai Typhoon Institute (STI) of China Meteorological Administration (CMA), including intensities (the maximum near-surface 2-min

Time	TS (CAT = 2, 17.2–24.4 m s^{-1})	STS (CAT = 3, 24.5–32.6 m s^{-1})	TY (CAT = 4, 32.7–41.4 m s^{-1})	STY (CAT = 5, 41.5–50.9 m s^{-1})	SuperTY (CAT = 6, ≥51 m s^{-1})
−24 h (t = −24)	30 (26.09%)	14 (12.17%)	39 (33.91%)	19 (16.52%)	13 (11.31%)
−18 h (t = −18)	27 (22.69%)	22 (18.48%)	39 (32.77%)	20 (16.81%)	11 (9.25%)
−12 h (t = −12)	28 (23.33%)	20 (16.67%)	40 (33.33%)	22 (18.34%)	10 (8.33%)
−6 h (t = −6)	23 (19.17%)	24 (20.00%)	41 (34.17%)	26 (21.66%)	6 (5.00%)
0 h (t = 0)	28 (24.13%)	25 (21.55%)	37 (31.90%)	22 (18.97%)	4 (3.45%)
6 h (t = +6)	42 (39.62%)	32 (30.19%)	28 (26.42%)	3 (2.83%)	1 (0.94%)
12 h (t = +12)	46 (51.11%)	25 (27.78%)	18 (20.00%)	0	1 (1.11%)
18 h (t = +18)	42 (59.15%)	17 (23.94%)	11 (15.49%)	1(1.41%)	0
24 h (t = +24)	40 (72.73%)	8 (14.54%)	7 (12.73%)	0	0

Note: The intensity is defined as the maximum sustained 10-m wind speed.

Table 1. Samples and frequencies of TCs with intensity of five categories (CAT = 2–6) from 24 h prior to landfall (t = −24), at the time of landfall (t = 0), to 24 h after landfall (t = 24) at every 6 h.

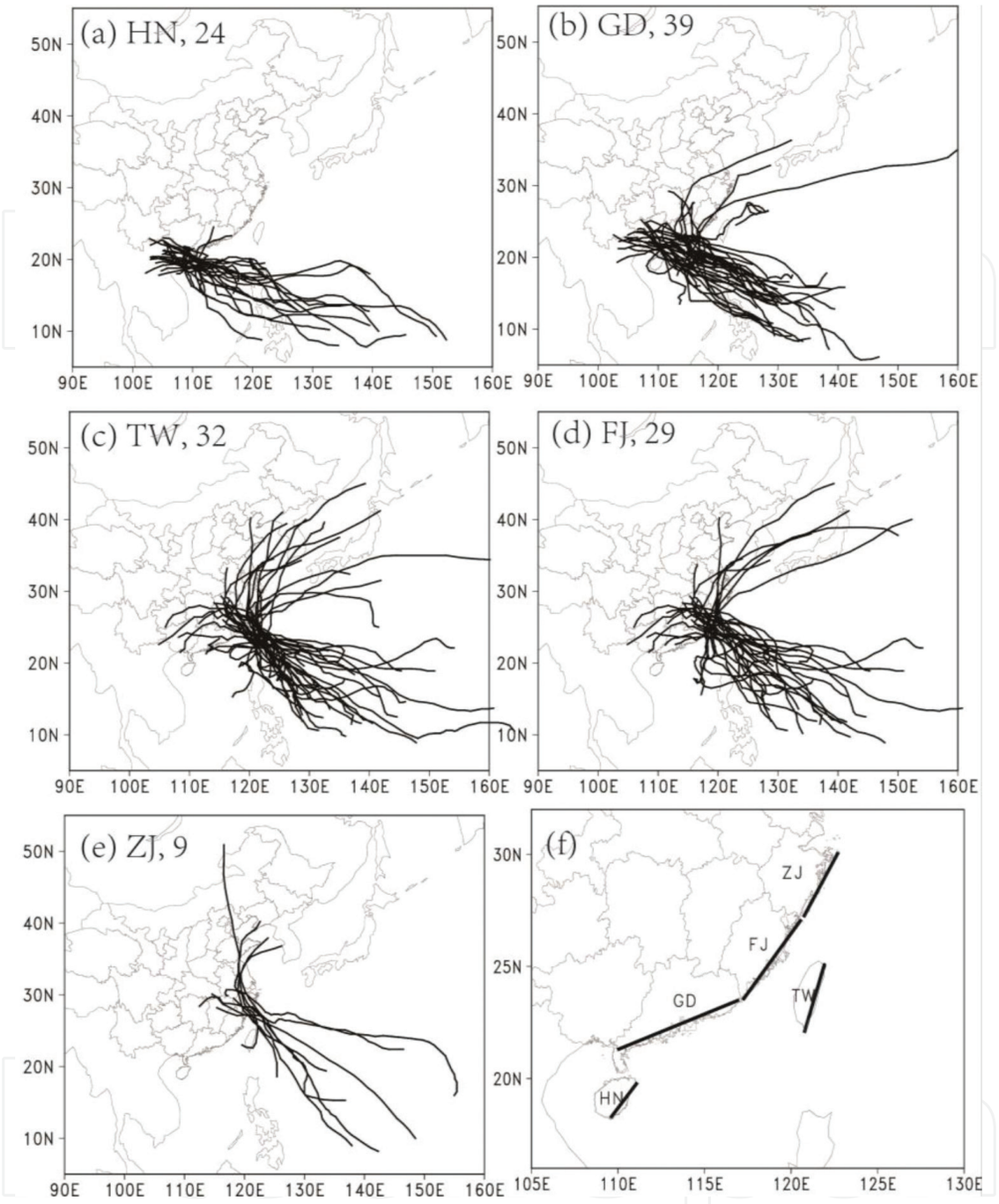

Figure 1. Tracks of TCs that made landfall in different regions (provinces) over China during 2001–2015: (a) Hainan (HN), (b) Guangdong (GD), (c) Taiwan (TW), (d) Fujian (FJ), and (e) Zhejiang (ZJ). Numbers of TCs making landfall in individual regions are illustrated in each panel. The names and locations of the five regions and their coastlines are shown in (f).

mean wind speed and the minimum sea-level pressure) and positions (longitude and latitude) of TCs at every 6-h interval during 2001–2015. **Table 1** shows the related 6-h intensity information including category, sample, and frequency of LTCs over China from t = −24 h to t = 24 h. The motion direction and speed of each TC at every TRMM observational time are calculated through the two nearest best-track records at 6-h interval. The intensity of a TC at landfall time is

obtained by interpolation using the maximum near-surface wind speed in the best-track data at 6-h interval.

Table 2 lists the intensity change information (including the calculation methods and samples). The intensity changes of LTCs are categorized into five groups: rapidly decaying (RD), slowly decaying (SD), unchanged, slowly intensifying (SI), and rapidly intensifying (RI), according to the rate of TC intensity change. The RI threshold of 15 m s^{-1} is defined as the 24-h maximum wind speed change, while the RD threshold is defined as −15 m s^{-1} in the 24-h intensity change [64]. As a result, the TCs of RI, SI, unchanged, SD, and RD have the 24-h intensity changes of ≥15, (0, 15), 0, (−15, 0), and ≤ −15 m s^{-1}, respectively. Note that the unchanged category is exactly defined as 0 m s^{-1}, and it occurs rather frequently, particularly within 24 h before landfall.

2.4. Rainfall analysis method

Fourier decomposition, which can help to compute the WN-0 and higher WNs (e.g., 1–4) rainfall components in a TC, is often used in the studies of rainfall distributions in TCs [23, 24]. The axisymmetric rainfall component is the azimuthally mean rain rate (WN-0) as a function of the radial distance in 10-km-wide annuli from the TC center. The asymmetric rainfall components were analyzed by binning rainfall rate data in 10-km-wide annuli from each TC center to 500-km radius. First, the WN-1 Fourier coefficients were computed by using all rain rate estimates as in Boyd [65]:

$$a_1 = \sum_i \left[R_i \cos\left(\theta_i\right)\right], b_1 = \sum_i \left[R_i \sin\left(\theta_i\right)\right], \quad (1)$$

Time	RI (ΔV ≥ 15 m s^{-1}, 24 h)	SI (ΔV = 0–15 m s^{-1}, 24 h)	Unchanged (ΔV = 0 m s^{-1}, 24 h)	SD (ΔV = −15–0 m s^{-1}, 24 h)	RD (ΔV ≤ −15 m s^{-1}, 24 h)
−24 h (t = −24)	3	73	26	16	0
−18 h (t = −18)	4	71	21	23	0
−12 h (t = −12)	4	67	17	31	0
−6 h (t = −6)	5	52	30	33	2
0 h (t = 0)	5	34	21	60	3
6 h (t = +6)	0	13	10	80	15
12 h (t = +12)	0	5	8	73	28
18 h (t = +18)	0	4	2	69	33
24 h (t = +24)	0	4	1	64	29

Note: △V is change in the maximum sustained 10-m wind speed.

Table 2. Samples of TCs with intensity change of five categories (RI, SI, unchanged, SD, RD) from 24 h prior to landfall (t = −24), at the time of landfall (t = 0), to 24 h after landfall (t = 24) at every 6 h.

where R_i is each of the individual rain rate estimates and θ_i is the phase angle of the estimate relative to either the storm motion or the VWS vector. The WN-1 asymmetric rainfall component (M_1) can be represented by

$$M_1 = \left[a_1 \cos(\theta) + b_1 \sin(\theta)\right]/R. \quad (2)$$

Similarly, the WNs 2–4 asymmetric rainfall components can be calculated respectively.

The shear-relative rainfall asymmetry is defined as the TRMM observed rainfall asymmetry relative to the VWS vector. Similarly, the motion-relative (or coastline-relative) rainfall asymmetries are composite of asymmetric rainfall relative to the motion direction (or coastline orientation) over every TRMM observation. The relative importance of the different factors on the asymmetric rainfall distribution can be characterized.

3. Axisymmetric rainfall

Based on the TRMM 3B42 rainfall data, the amplitude of the WN-0 (axisymmetric component) rainfall is about 0.4–0.6 of the total rainfall in general, though there are some subtle differences in various regions (**Figure 2**). This means that the axisymmetric component could explain about half of the variance of the total rainfall. For a comparison, **Figure 2** also shows the amplitudes of different WN components. The amplitude of the WN-1 component is about 0.2, while the amplitudes of the WN-2, WN-3, and WN-4 components are all less than 0.2 and show smaller and smaller values with the higher WNs. This suggests that on average the axisymmetric component is dominant of the total rainfall and the WN-1 component dominates in the asymmetric rainfall in LTCs. Another feature in **Figure 2** is that there is a large axisymmetric rainfall decrease for the LTCs after landfall in most studied regions over China.

3.1. Axisymmetric rainfall evolution during landfall

The axisymmetric rainfall distributions in LTCs before landfall and after landfall in the five regions of China shown in **Figure 1** are further compared in **Figure 3**. The peak rainfall is about 5.5 mm h^{-1} and located near 60 km from the TC center within 24 h before landfall (**Figure 3a**). After landfall, the peak rain rate is reduced to about 3 mm h^{-1} and located much closer to the TC center (**Figure 3b**). Therefore, the maximum mean axisymmetric rain rate is largely reduced and shifts inward during landfall likely because of the increased surface frictional convergence and the associated eyewall contraction or collapse [66]. Meanwhile, the azimuthally averaged radial profiles of rain rate vary with landfalling regions, which are similar to the radial profiles in the five different ocean basins of the globe as illustrated in [23].

3.2. TC intensity and averaged axisymmetric rainfall

The axisymmetric rainfall is tied to TC intensity on average. **Figure 4** shows the evolutions of TC intensity and the axisymmetric rainfall rate in LTCs in the five regions of China. Generally during

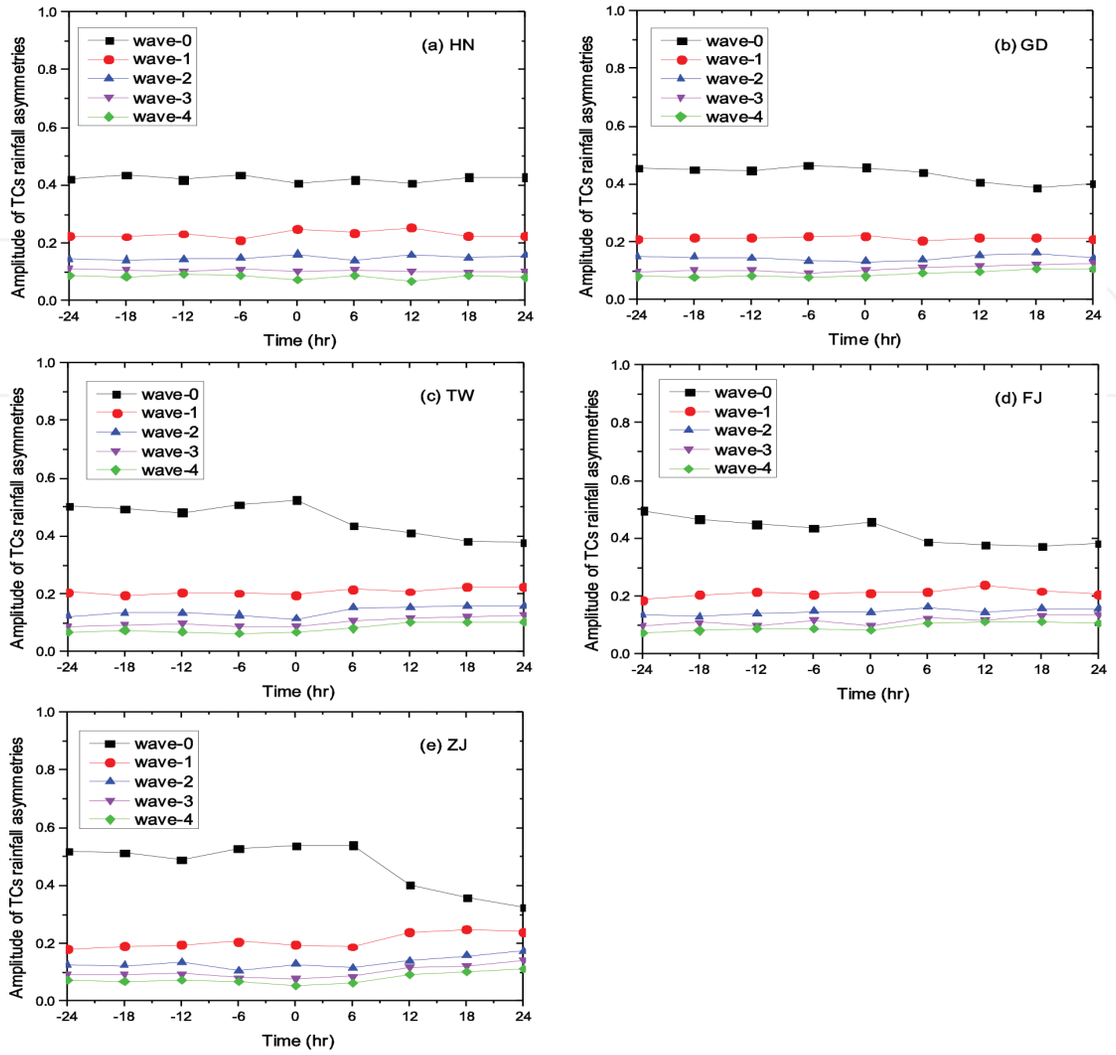

Figure 2. The 6-h amplitudes (×100%) of the WN-0 (axisymmetric) and WN-1, WN-2, WN-3, and WN-4 (asymmetric) components of TC rainfall relative to the total rainfall in regions of (a) HN, (b) GD, (c) TW, (d) FJ, and (e) ZJ from 24 h prior to landfall to 24 h after landfall.

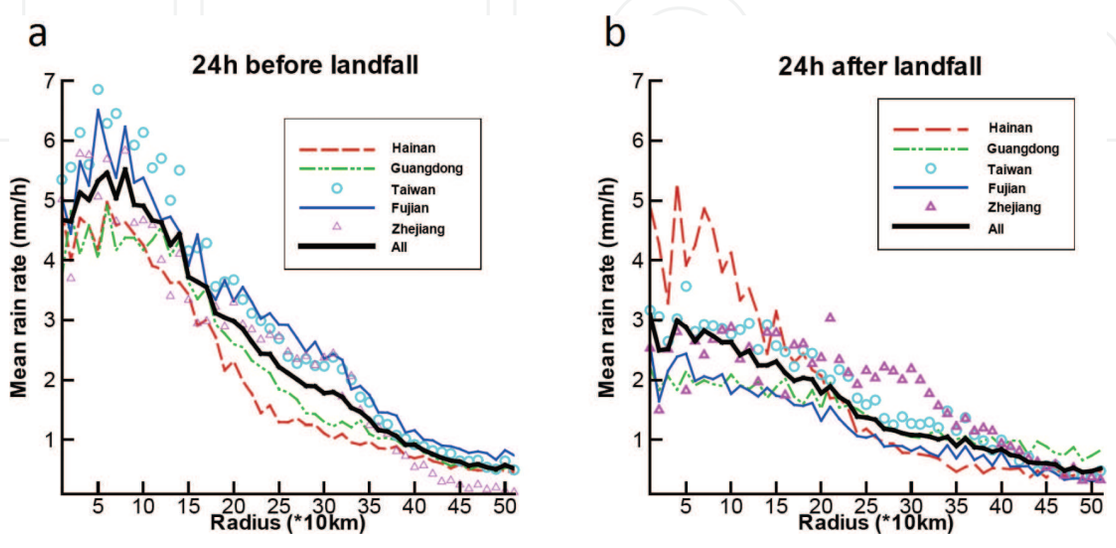

Figure 3. Radial profiles of the azimuthally averaged rain rates in TCs making landfall in different regions (a) 24 h prior to landfall and (b) 24 h after landfall.

24–12 h (t = −24 to −12) prior to landfall, most TCs is still intensifying, but starts to weaken at the time of landfall (t = 0) (**Figure 4a**). During the landfall process (from t = −24 to t = +24), the mean TC maximum wind speed is decreased from 34 to 20 m s^{-1}, namely about 41% decrease in 48 h, while the mean TC minimum sea-level pressure increases from 970 to 992 hPa (**Figure 4b**). During this period, the averaged axisymmetric rain rate shows a very similar variation with the rain rate decreased by about 38% in 48 h (**Figure 4c**). This suggests that the axisymmetric rain rate is positively correlated with TC intensity. In addition, with the decreased intensity of the TCs during landfall, the mean axisymmetric rain rate decreases within a radius of 150 km from the TC center (**Figure 4d**).

3.3. TC intensity and maximum total rain, rain area, and rain rate

Although the axisymmetric rainfall in LTCs is positively correlated with TC intensity, the extreme rainfall parameters in terms of various metrics are not necessarily related perfectly to TC intensity. Here to demonstrate such features, 3 parameters are defined: maximum rain rate (the largest rain rate over all grid points within 500 km of each TC center),

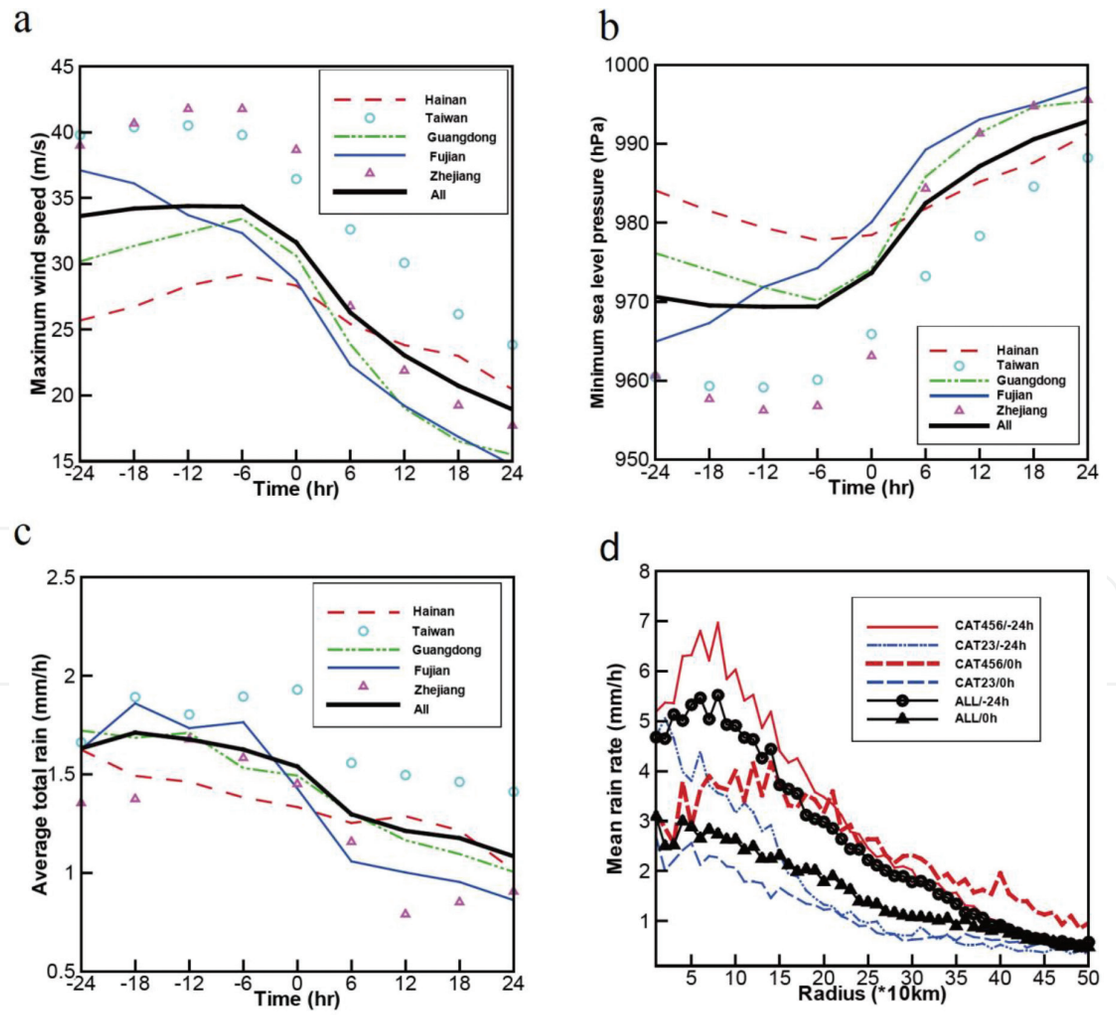

Figure 4. Evolution of rainfall from 24 h prior to landfall to 24 h after landfall at 6-h intervals for (a) the averaged intensity indicated by the maximum sustained 10-m wind speed, (b) the averaged minimum sea-level pressure, and (c) the areal averaged rain rate within 500-km radius of the TC center for all TCs. (d) Radial profiles of the azimuthally averaged rain rates for different TC intensity categories.

maximum total rain (the largest value of accumulated rainfall within 500 km of the TC center among CAT2–6 TC samples), and maximum area of rain (the largest value of fractional rain area relative to the TC area within 500 km radius from the TC center among CAT2–6 TC samples).

As shown in **Figures 5–6**, on average, the CAT6 TCs have the highest rain rate (**Figure 5a**), the highest total rain (**Figure 5b**), and the largest rain area (**Figure 6**), while the CAT2 TCs have the lowest rain rate (**Figure 5a**), the lowest total rain (**Figure 5b**), and the smallest rain area (**Figure 6**).

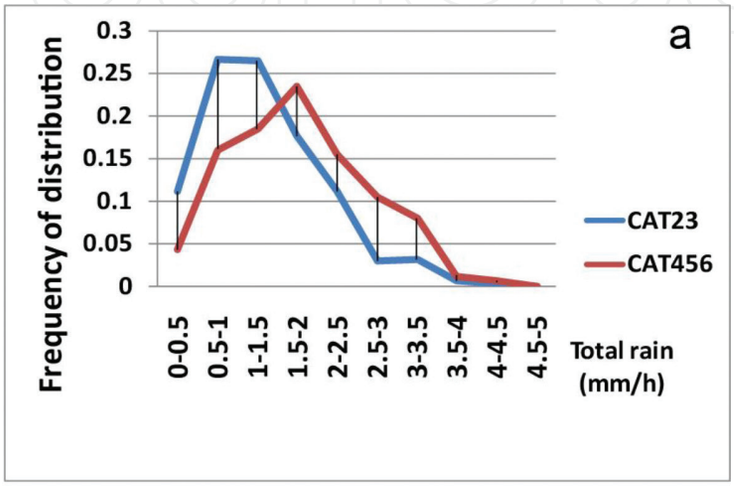

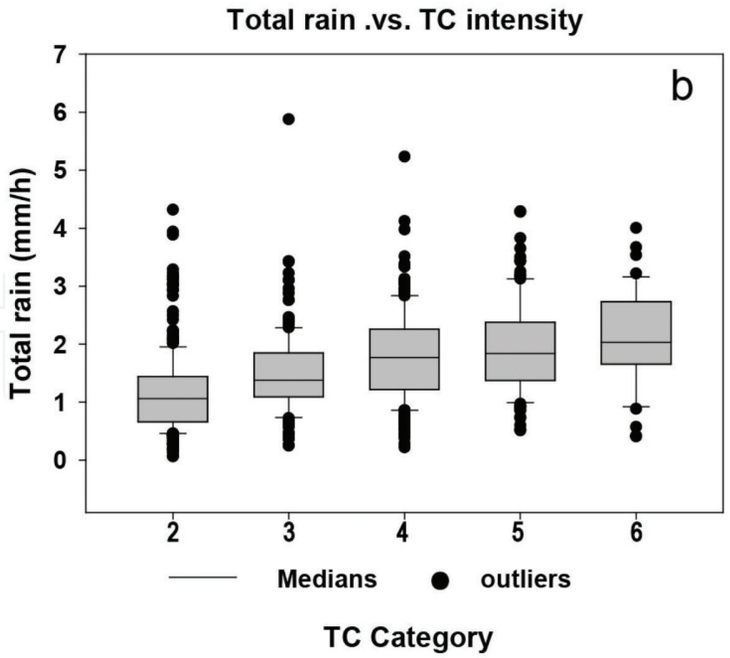

Figure 5. (a) Frequencies of the total rain (the areal averaged rain rate within 500-km of the TC center) for CAT23 and CAT456 TCs. (b) the total rain distributions for TC categories of CAT2–6 from 24 h prior to landfall to 24 h after landfall (medians and outliers in the box plots have the same meaning later).

http://dx.doi.org/10.5772/intechopen.75910

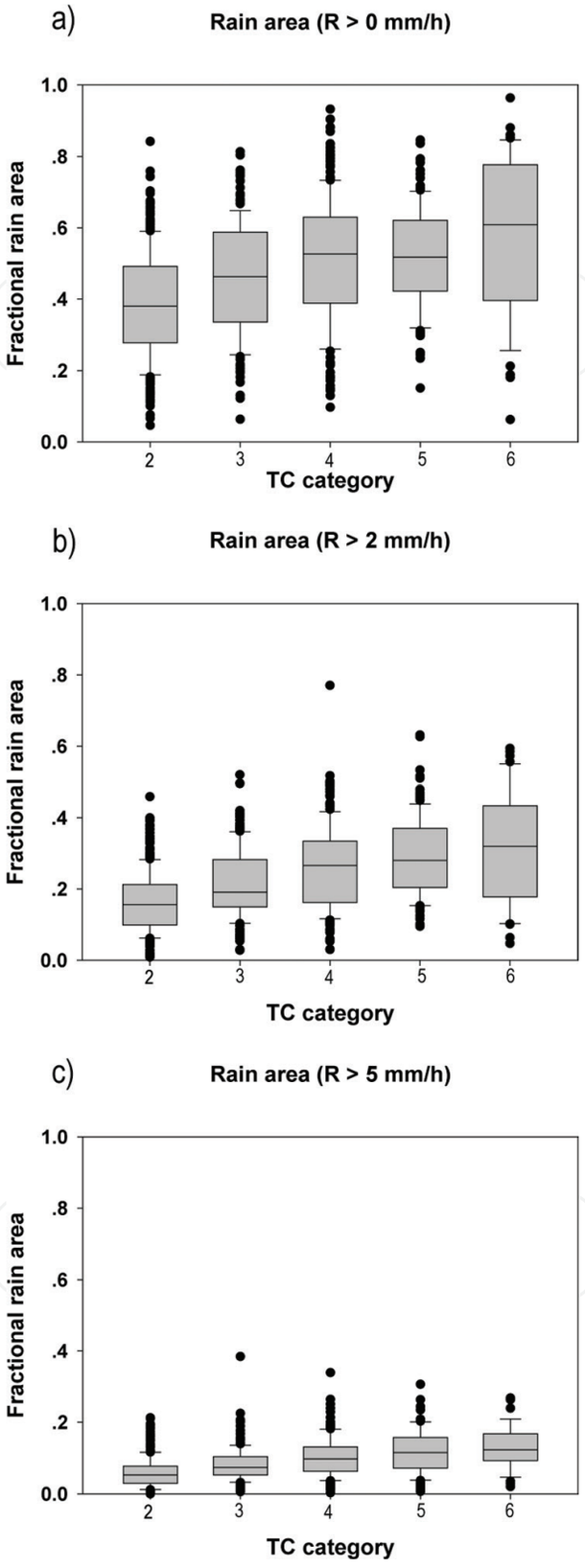

Figure 6. Fractional rain area (×100%) relative to the total area within a 500-km radius from the TC center with different rain rates: (a) R > 0, (b) 2, and (c) 5 mm h^{-1} for TC categories of CAT2–6 from 24 h prior to landfall to 24 h after landfall.

Figure 7a also shows the averaged rain area evolutions of three various rain rates for LTCs of CAT456 and CAT23 during landfall. For both strong and weak TCs, the rain area would shrink to about 10% of the total rain area with the rain rate increasing to being greater than 5 mm h^{-1}. However, the weaker TCs like CAT2 TCs have larger extreme values of the maximum rain

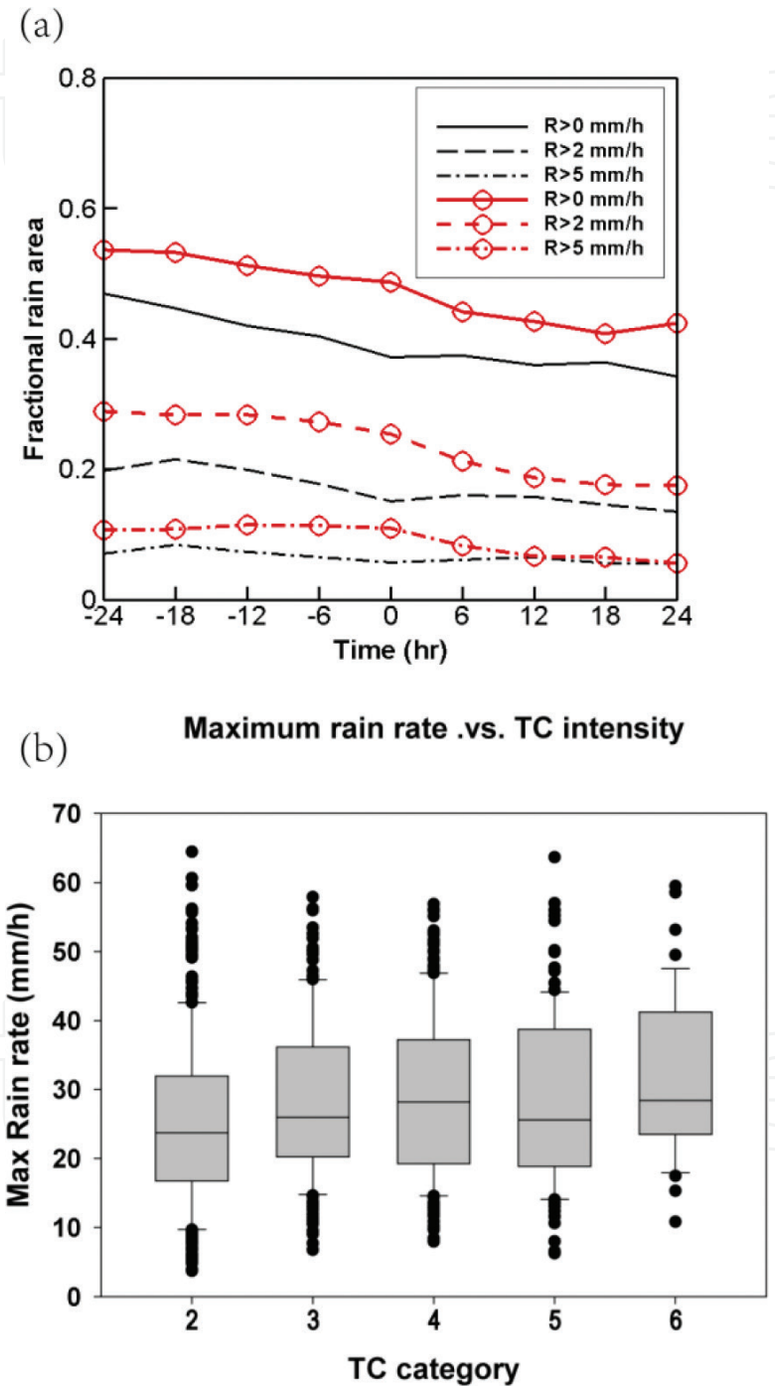

Figure 7. (a) The fractional rain area (×100%) of the total area within a 500-km radius of the TC center with different rain rates >0, 2, 5 mm h^{-1} for CAT456 (with red circles) and CAT23 TCs (without circles) from 24 h prior to landfall to 24 h after landfall. (b) The maximum rain rate (mm h^{-1}) within a 500-km radius of the TC center for TCs of CAT2–6 from 24 h prior to landfall to 24 h after landfall.

rate, total rain, and rain area (**Figures 5b**, **6**, and **7b**). This result thus suggests that the averaged rain features (including rain rate and rain area) are all related to TC intensity, but the extreme rain features (including the maximum rain rate and rain area) are not necessarily so.

3.4. TC intensity change and the axisymmetric rain change

Since the axisymmetric rainfall is related with TC intensity in LTCs, the TC intensity change would be also correlated to the rainfall change. It is shown in **Figure 8a** that on average, the

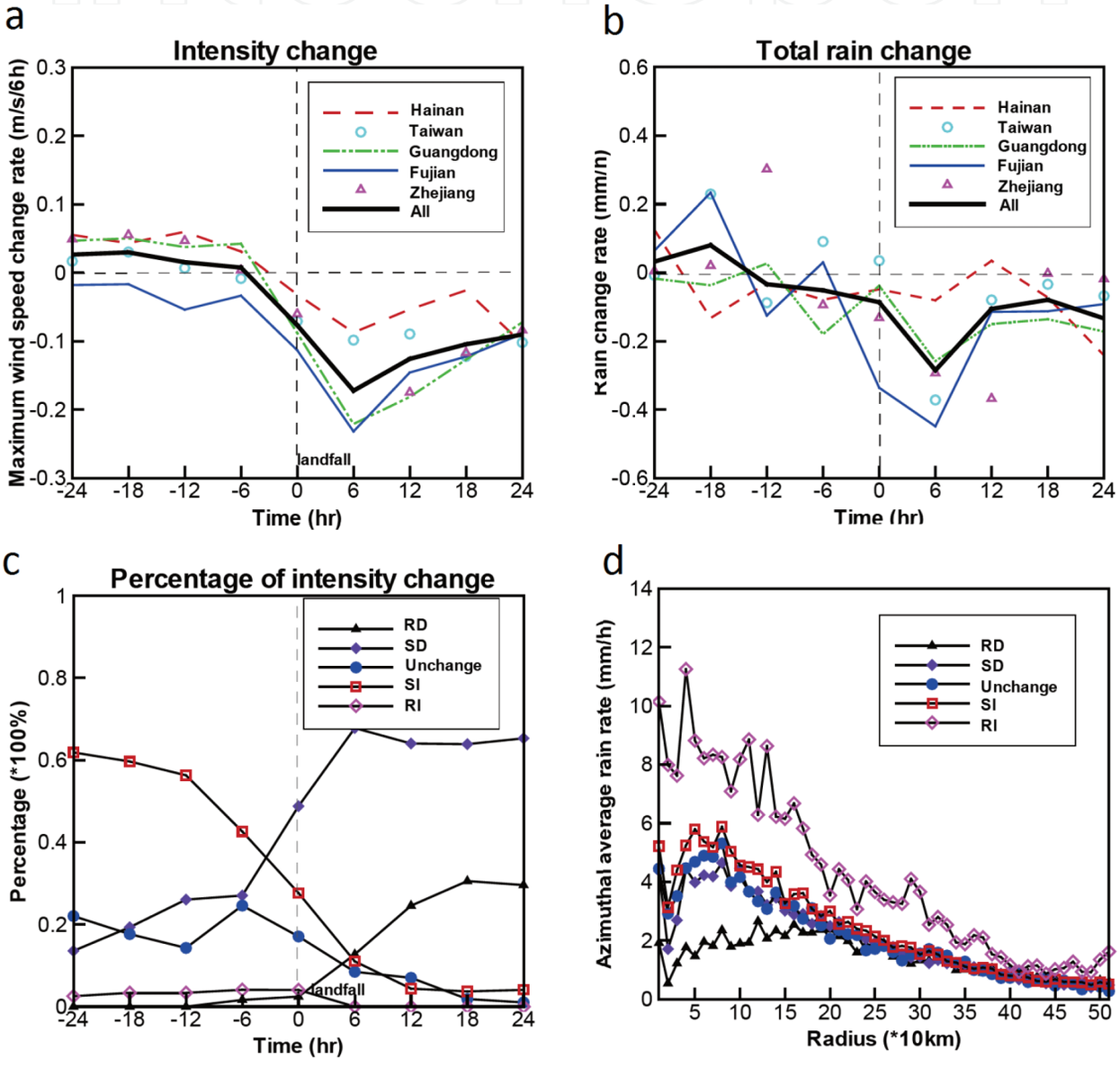

Figure 8. Six-hourly time evolution from 24 h prior to landfall to 24 h after landfall for (a) the rate of averaged TC intensity change (m s^{-1} in 6 h), (b) the rate of change of the areal averaged rain rate (within 500-km radius of the TC center; mm h^{-1}) for all TCs, and (c) the frequency of TCs of rapid decaying (RD), slow decaying (SD), unchanged, slow intensifying (SI), and rapid intensifying (RI). (d) Radial profiles of the azimuthally averaged rain rates for different intensity change groups.

rate of the averaged LTC intensity change is slightly positive or close to zero before landfall, but turns to be negative after landfall. Correspondingly, the rate of the averaged rain rate change presents a similar evolution during landfall (**Figure 8b**). As a result, the correlation coefficient between the LTC intensity change and the axisymmetric rain change reaches 0.77, indicating that they are highly correlated during landfall. **Figure 8c** shows that within 24 h before landfall, 70–90% of LTCs increase or maintain the intensity, while after landfall 20–30% of LTCs have RD process. During the 48-h landfall process, RI rarely occurs in LTCs. **Figure 8d** shows that LTCs of different intensity change categories have different radial distributions in their axisymmetric rain rate. The RI TCs have the highest mean peak axisymmetric rain rate (>13 mm h^{-1}) located at the smallest radius of near 40 km, while the RD TCs have the lowest peak axisymmetric rain rate (about 3 mm h^{-1}) at the radius of about 125 km from TC center. Note also that the total rain rate change from an increase to a decrease for TCs from RI to RD (**Figure 9**).

3.5. TC intensity and the axisymmetric contribution to the total rainfall

Figure 10 compares the axisymmetric contribution to the total rainfall between strong TCs (CAT456) and weak TCs (CAT23). The strong TCs have larger total rainfall in general (**Figure 10a** and **b**), also with a higher contribution from the axisymmetric rainfall component to the total rainfall than the weak TCs (**Figure 10c** and **d**). On average, the weak TCs have lower total rainfall with a larger contribution from the asymmetric components (including WNs 1–4) to the total rainfall.

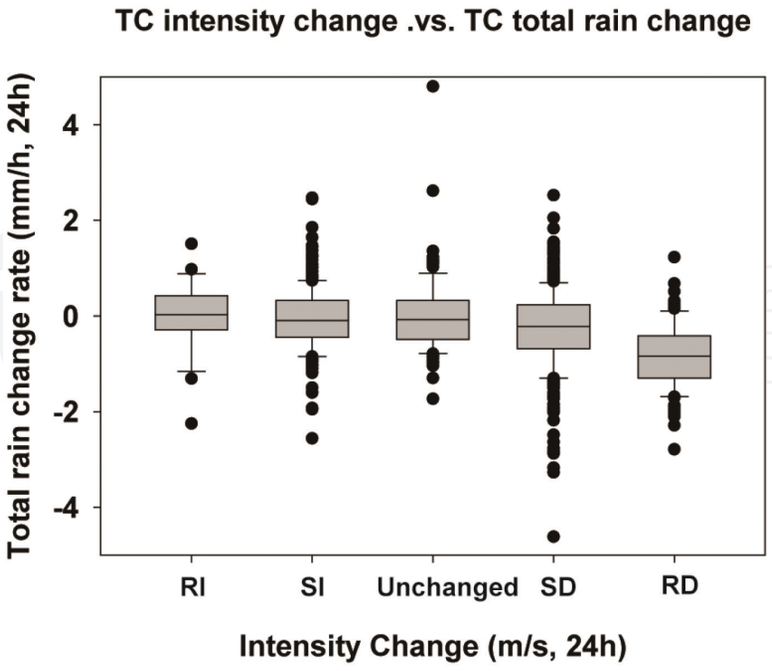

Figure 9. The relationship between different TC intensity change (RI, SI, unchanged, SD, and RD) and total rainfall change from 24 h prior to landfall to 24 h after landfall.

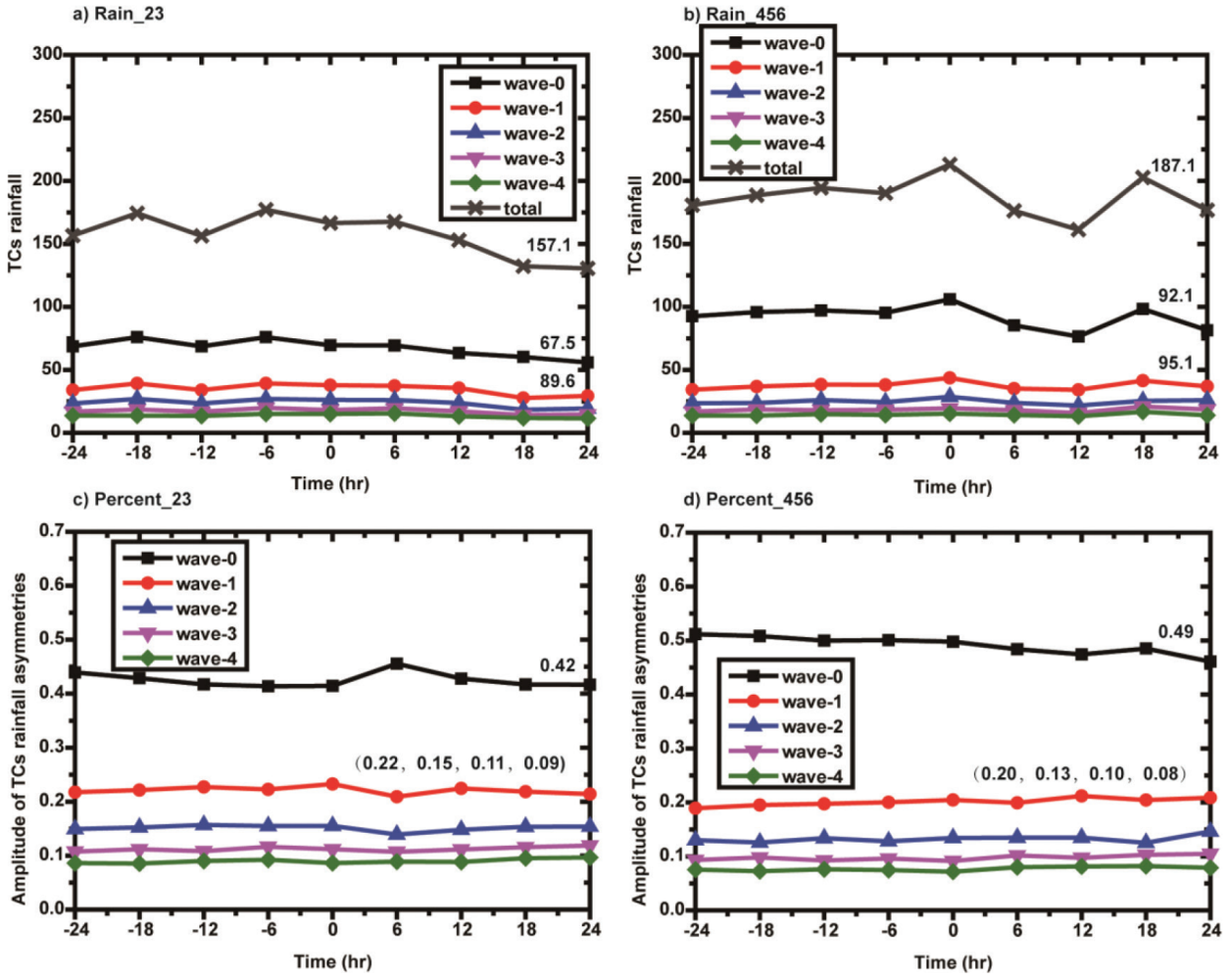

Figure 10. Time evolution of the 6-h WN-0, WN-1, WN-2, WN-3, and WN-4 rainfall components and the total rainfall (mm) from 24 h prior to landfall to 24 h after landfall for (a) CAT23 and (b) CAT456 TCs, and the time integrated mean values of total rainfall, WN-0, and asymmetric rainfall (WNs 1–4) are written above the curves in (a) and (b); (c) and (d) are, respectively, the same as (a) and (b) but for the 6-h amplitudes (×100%) of the WN-0, WN-1, WN-2, WN-3, and WN-4 rainfall components relative to the total rainfall. The time integrated mean values of amplitudes of WN-0, and asymmetric parts (WN-1, WN-2, WN-WN-3, and WN-4, respectively) are written above the curves in (c) and (d).

4. Asymmetric rainfall

Except for the dominant contribution of the axisymmetric component to the TC total rainfall, the asymmetric component, especially that from the WN-1, is also shown to be considerable in previous studies of Yu et al. [25, 26]. The WN-1 rainfall asymmetry in LTCs in the five regions of China (**Figure 11**) shows that the maximum rainfall was generally located in the south of TC center before landfall and slightly rotates cyclonically from HN, GD, TW, FJ to ZJ, namely, from South China to East China. This cyclonical rotation still exists after landfall with the maximum rainfall cyclonically rotated to the northeast in LTCs in ZJ of East China. The effects of some important factors including VWS, TC motion, intensity, and coastline on the LTC asymmetric rainfall distribution are also discussed below.

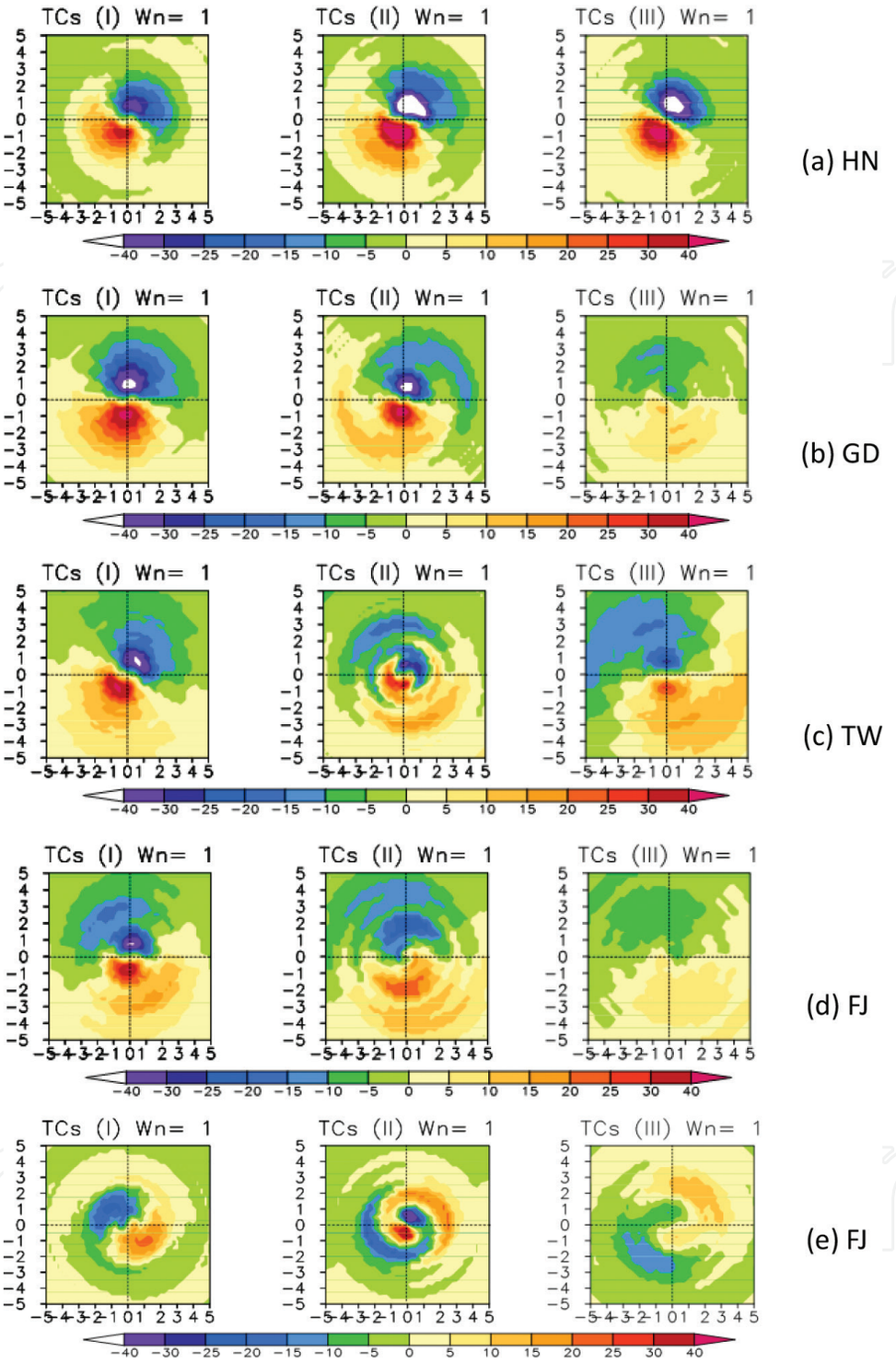

Figure 11. The WN-1 rainfall asymmetry (unit: mm) as a function of the distance from the TC center for TCs making landfall in different regions: (a) Hainan, (b) Guangdong, (c) Taiwan, (d) Fujian, and (e) Zhejiang in three stages. X and Y axes are the distance (degree) from the TC center (origins). Stage (I) is 24 h prior to landfall, stage (II) is at the time of landfall, and stage (III) is 24 h after landfall. The color scale indicates the amplitude of the asymmetry relative to the distance from the TC center.

4.1. Effect of vertical wind shear

Most LTCs in South China are still far away from the midlatitude westerlies, and therefore, in general no direct impacts of westerly troughs on LTCs occur. However, the LTCs in East

China are often close to the westerly systems (troughs and ridges) from the north, and thus they are more frequently and directly affected by the midlatitude westerlies so that the westerly trough would impinge into the LTC circulations. As a result, the high VWS, the water vapor flux channel, and the accompanied baroclinic zone often impose significant impact on rainfall distribution in the LTCs in East China, especially after landfall in Yu et al. [25].

Figure 12 shows the changes of the environmental VWS during 24 h before landfall to 24 h after landfall. It shows that prior to landfall, the LTCs are affected by easterly VWS for regions of HN, GD, TW, and FJ, while westerly VWS for ZJ region (as shown by green curves in **Figure 12**). After landfall, the averaged easterly VWS is generally decreased with time during landfall except for a strengthening of the averaged VWS and a variation from westerly VWS to southwesterly VWS for ZJ region (as shown by red curves in **Figure 12**). Therefore, there exists a cyclonic rotation of VWS for the LTCs from South China to East China both prior to and after landfall.

The shear-relative WN-1 rainfall distribution in TCs making landfall in the five regions from South China to East China confirms that the asymmetric rainfall maximum in LTCs in all five regions is mainly located downshear to downshear-left whenever 24 h prior to landfall, or at the time of landfall, or 24 h after landfall (facing down the VWS vector aligned with the positive Y-axis in **Figure 13**). The cyclonic rotations of the rainfall maximum in the LTCs in the five regions are thus closely related to the cyclonic rotation of VWS. This indicates that VWS is a dominant factor affecting the asymmetric rainfall distribution in TCs; regardless the TCs are over open oceans or making landfall.

4.2. Effects of TC intensity

When the TCs are separated into two groups of CAT23 (weak TCs) and CAT456 (strong TCs) based on their intensity, we can find that in both CAT456 and CAT23 TCs, the maximum rainfall is always located downshear to downshear-left during landfall from t = −24 to t = 24 (**Figure 14**). However, the mean VWS magnitude for CAT23 TCs is 8.6 m s^{-1}, which is larger than 6.0 m s^{-1} for CAT456 TCs. The rainfall maximum in CAT456 TCs is a little bit cyclonically rotated from the VWS vector relative to that in CAT23 TCs. This might be related to the differences in both the VWS magnitude and the TC intensity. First, for strong VWS and weak TCs, the location of rainfall maximum is often located in downshear to downshear-left quadrant when facing downshear direction. But for weak VWS and strong TCs, the rainfall maximum could rotate further cyclonically to the downshear-left or even to the left of the shear vector. This indicates the relationship between VWS and rainfall asymmetry is determined not only the magnitude of the VWS but also the TC intensity.

4.3. Effect of TC motion

During the landfall period from 24 h prior, to landfall, and to 24 h after landfall, the motion-relative WN-1 rainfall maximum in LTCs in the five regions of China shows large variability (facing down the TC motion vector aligned with the positive Y-axis in **Figure 15**). The rainfall maximum for LTCs in HN is often to the left of the motion vector, while for LTCs in FJ the rainfall maximum occurs in the rear side of the motion vector. This indicates that the rainfall asymmetry may not be predominantly controlled by the TC motion vector for LTCs over China.

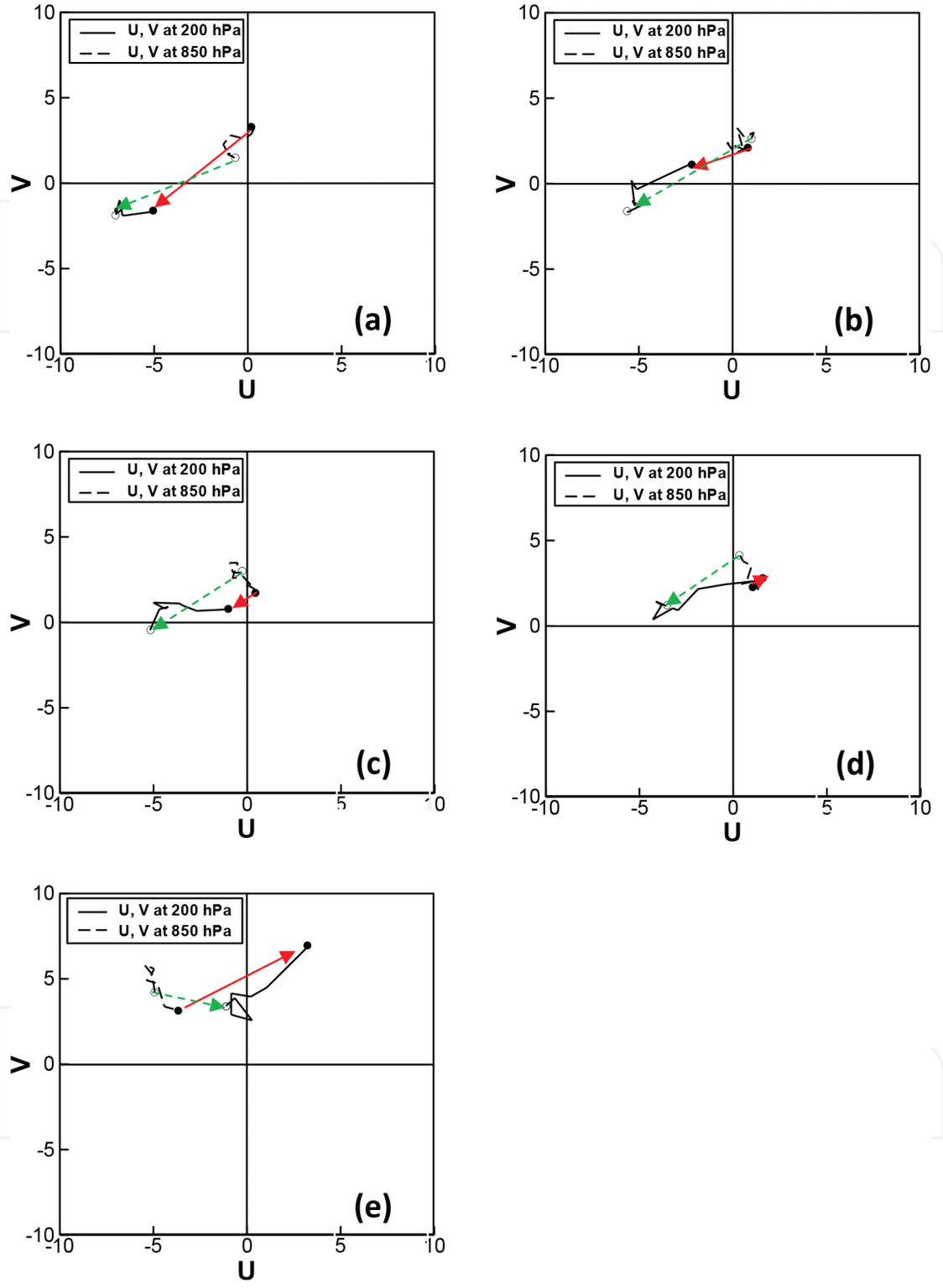

Figure 12. Changes in the averaged zonal wind (U, unit: m s^{-1}) and meridional wind (V, unit: m s^{-1}) within 500 km of the TC center for TCs making landfall in (a) Hainan, (b) Guangdong, (c) Taiwan, (d) Fujian, and (e) Zhejiang. The open and solid circles represent the 9 points (at every 6 h) starting at 24 h prior to landfall and ending at 24 h after landfall, respectively. The black solid lines are wind changes at 200 hPa, and the black long dashed lines are wind changes at 850 hPa. The green (red) dash lines represent the vertical wind shear at 24 h prior to (24 h after) landfall.

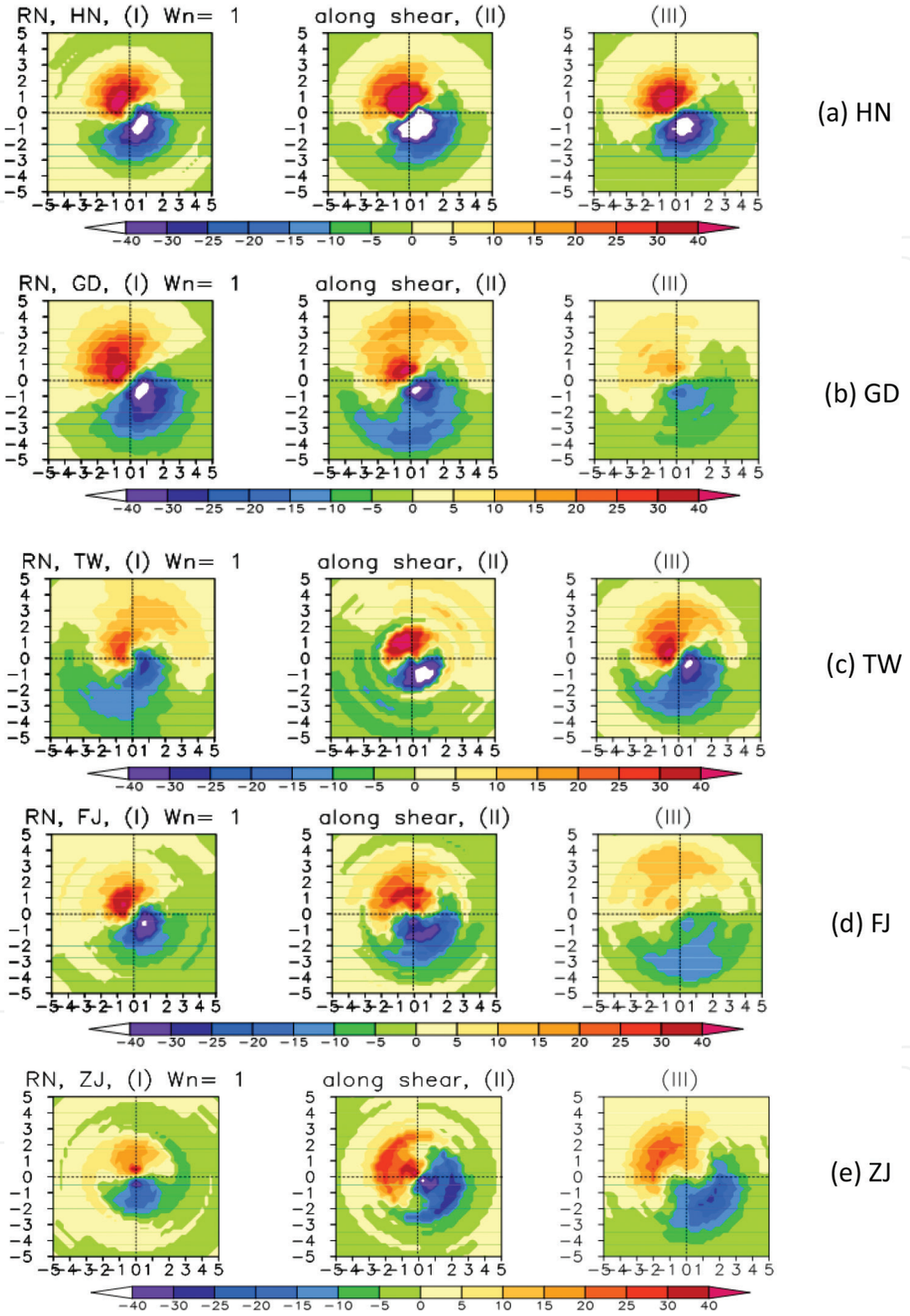

Figure 13. Same as in **Figure 11** but for the WN-1 rainfall asymmetry (unit: mm) relative to the VWS. The shear vector is aligned with the positive Y-axis (upward). X and Y axes are distance (in degree) from the TC center (origins). (I), (II), and (III) are 24 h prior to landfall, at the time of landfall, and 24 h after landfall, respectively. The color scale indicates the amplitude of the asymmetry relative to the VWS.

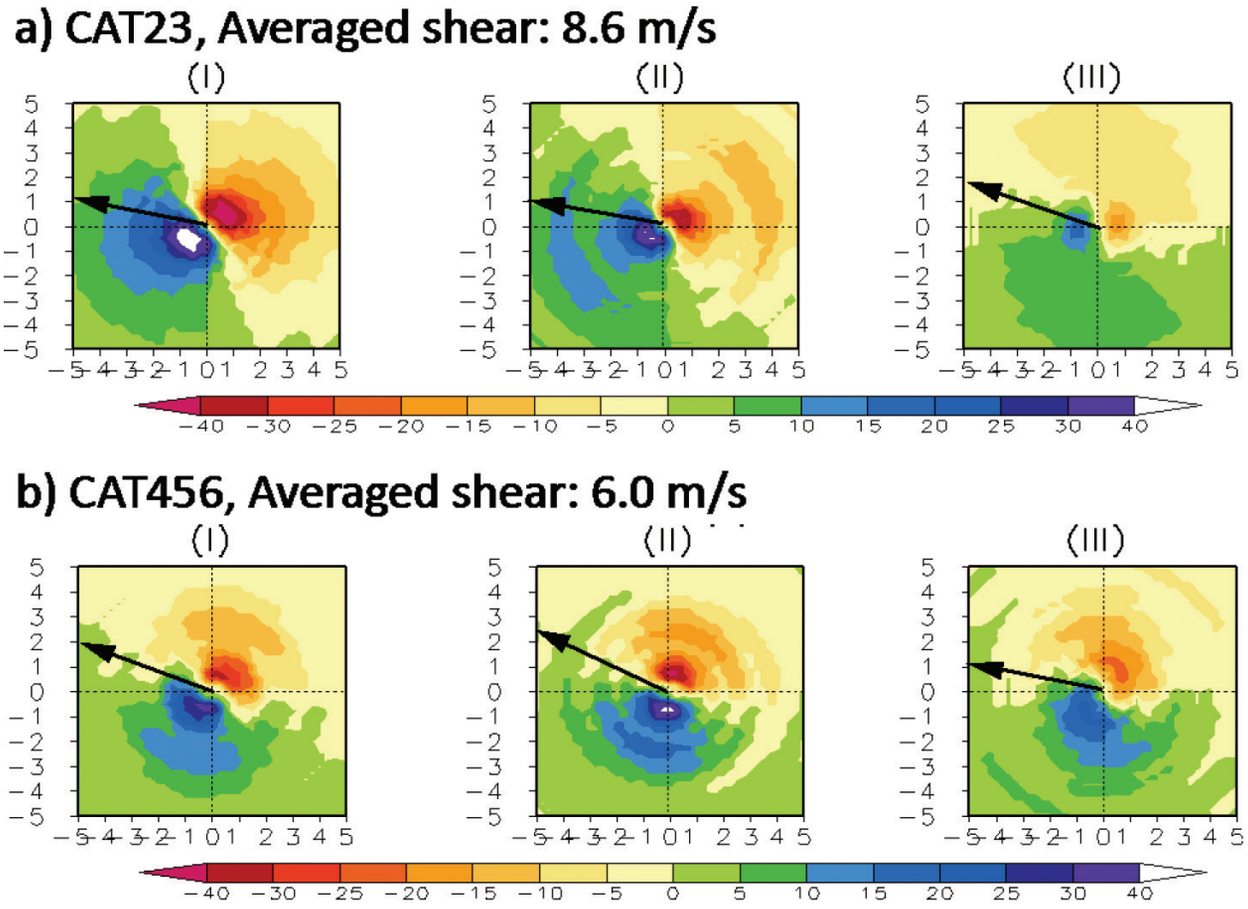

Figure 14. The WN-1 rainfall asymmetry (shaded, mm) for (a) CAT23 and (b) CAT456 TCs. The solid arrows denote the averaged VWS vector. X and Y axes are distances in longitude and latitude (in degree) from the TC center (origin). (I), (II), and (III) are 24 h prior to landfall, at the time of landfall, and 24 h after landfall.

In addition to the motion direction, the motion speed shows inconsistent relationship with rainfall asymmetry as well. **Figure 16** shows rainfall asymmetries in TCs of three different translational speeds: less than 12, 12–20 km h^{-1}, and larger than 20 km h^{-1}. We can see that regardless of different motion speeds, the maximum rainfall is predominantly located in the left and even rear-right quadrants when facing down the TC motion vector. This means that the TC motion speed has no obvious impacts on the rainfall asymmetric distribution in LTCs over China. This may partly suggest that the effects of storm motion on the asymmetric rainfall distribution in the studied regions are dominated by the effects of environmental VWS.

4.4. Effects of coastlines

In contrast to the negligible effects by LTC motion, the WN-1 rainfall maximum is strongly affected by the coastlines, especially in the LTC outer core region and at the time of landfall. **Figure 17** shows the WN-1 rainfall asymmetries for LTCs with different magnitudes of VWS (less than 5, 5–7.5 m s^{-1}, and larger than 7.5 m s^{-1}, respectively). In the inner core region (within a radius of 2° of latitude), the maximum rainfall in LTCs is generally located offshore and downshear-left under all VWS conditions during landfall. However, in the outer core

http://dx.doi.org/10.5772/intechopen.75910

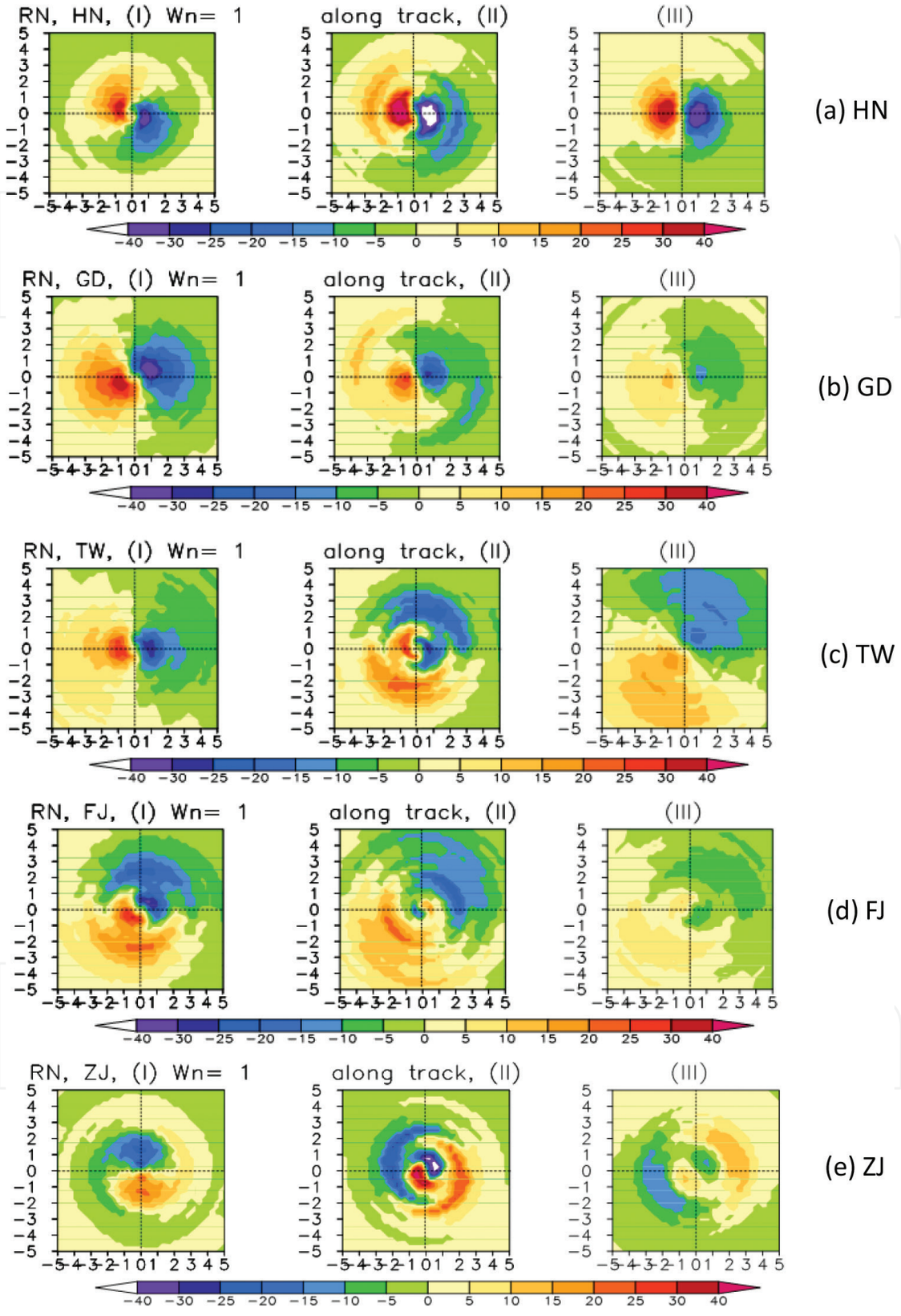

Figure 15. Same as in **Figure 13** but for the WN-1 rainfall asymmetry (unit: mm) relative to the TC motion. The motion vector is aligned with the positive Y-axis (upward). X and Y axes are distance (degree) from the TC center (origins). (I), (II), and (III) are 24 h prior to landfall, at the time of landfall, and 24 h after landfall. The color scale indicates the amplitude of the asymmetry relative to the TC motion.

region (between 2 and 5° of latitude from the TC center), the asymmetric rainfall maximum is rotated cyclonically from offshore gradually to the onshore in TCs under decreasing environmental effects from strong VWS to weak VWS (namely, from larger than 7.5 m s^{-1} to less than 5 m s^{-1}). This result is consistent with that previously reported in a numerical study of Xu et al. [45], which showed that the land-sea surface contrast could produce an increase in the rainfall percentage onshore in a LTC. Results in Yu et al. [26] showed that when the VWS is very weak, the land-sea contrast could predominantly contribute to the rainfall asymmetry. Nevertheless, the situation could become more complicated under weak VWS, because other factors including the coastline and storm motion might play their roles together to determine the asymmetric rainfall distribution in LTCs, particularly in the TC outer core and at time of landfall.

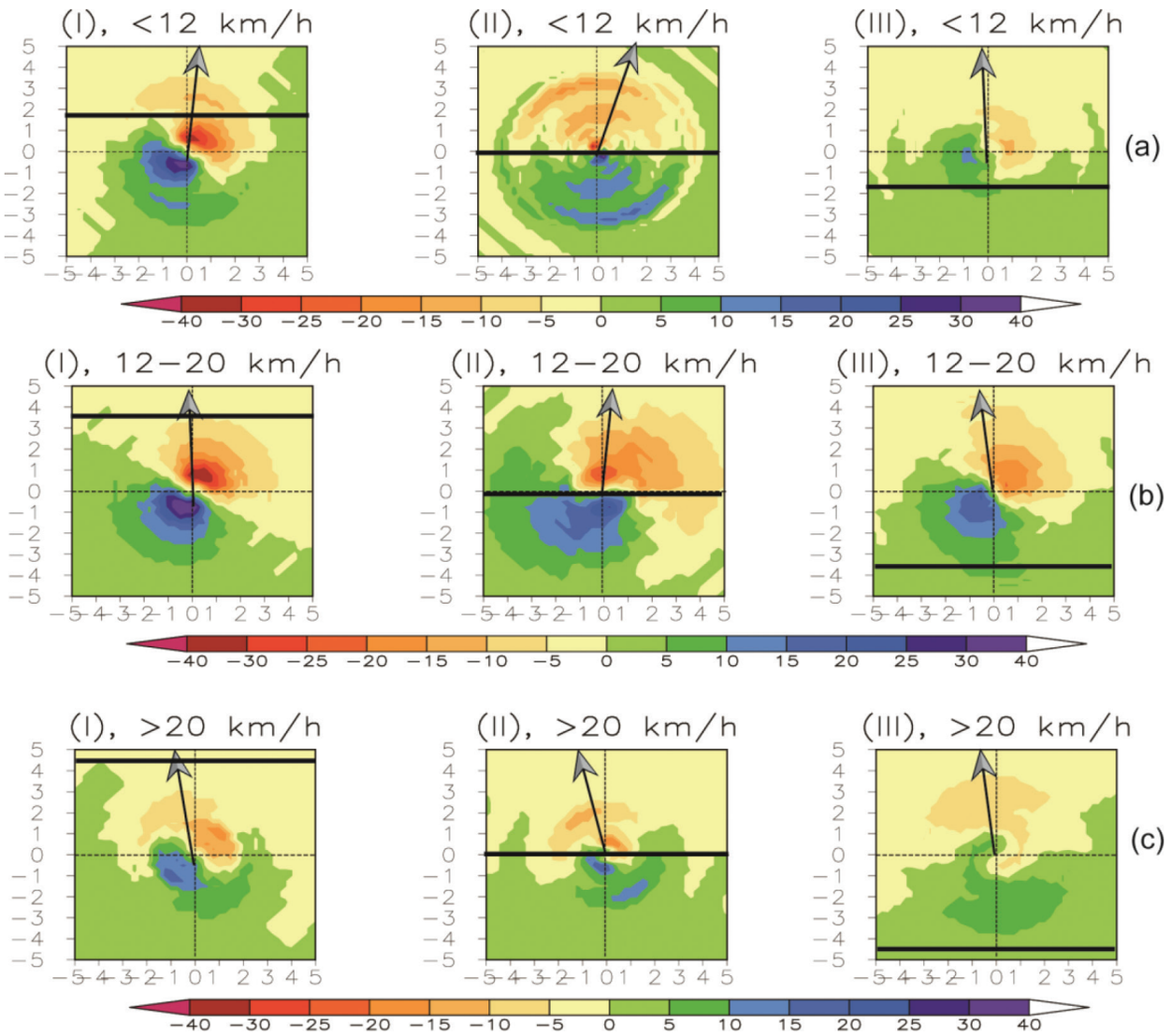

Figure 16. The WN-1 rainfall asymmetry (shaded, mm) relative to the coastlines for TCs with different translational speeds: (a) <12 km h^{-1}, (b) 12–20 km h^{-1}, and (c) > 20 km h^{-1}. The coastline is aligned with the positive X-axis to the right (shown by the black solid lines) and the arrows denote the mean motion direction.

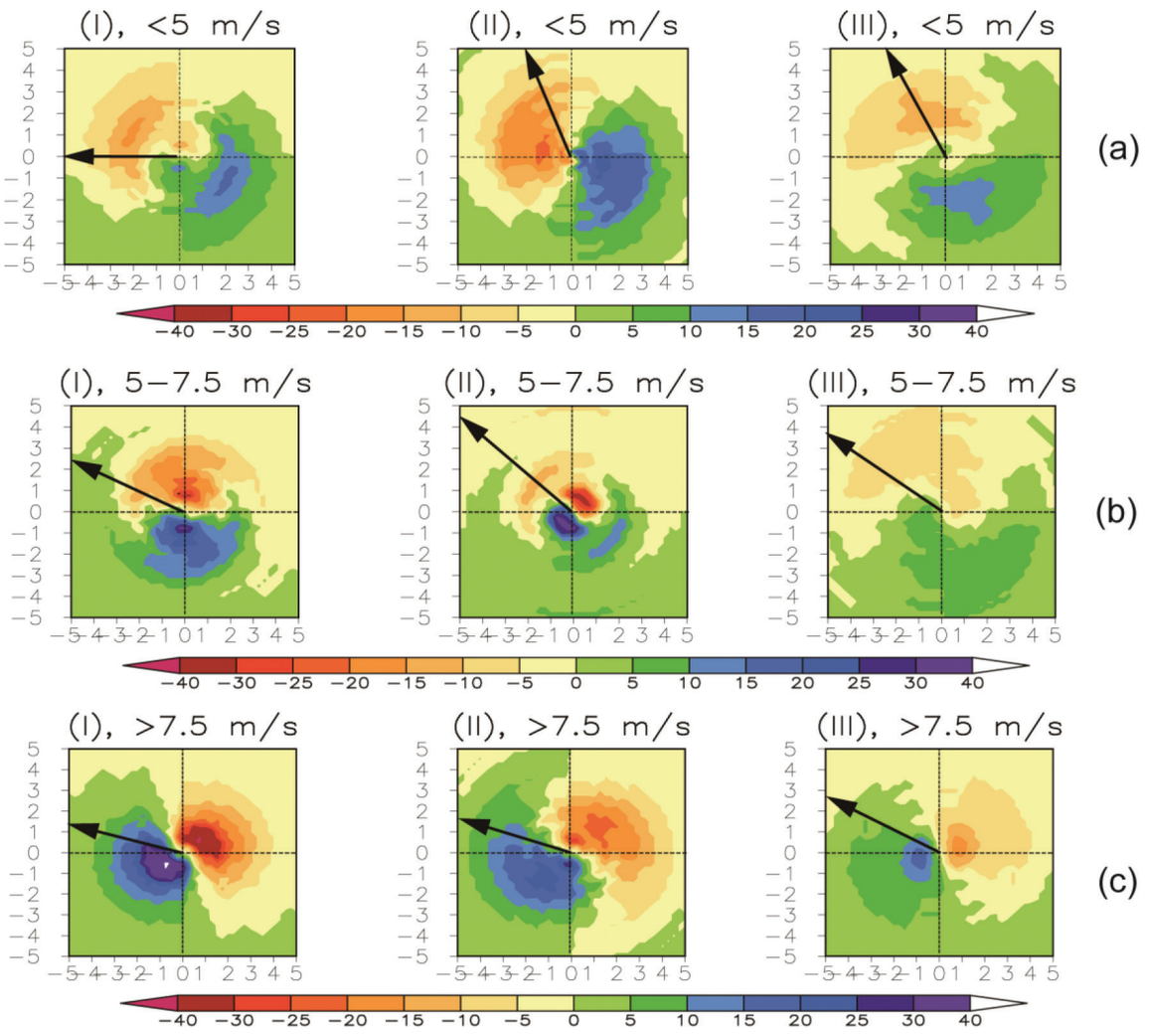

Figure 17. Same as in **Figure 16** but for TCs with different VWS magnitudes: (a) <5 m s^{-1}, (b) 5–7.5 m s^{-1}, and (c) >7.5 m s^{-1}. The solid arrows denote the averaged VWS vectors.

5. Case studies

Since LTC rainfall involves complicated process, such as multi-scale interactions with various scale motions in the environment, coastline, orography, as well as the structure and intensity of the storm itself, detailed case studies can help to deepen our understanding of the various processes that are essential to the rainfall distribution in LTCs. Here two recent case studies are briefly discussed as an illustration how important the cold pool dynamics and the baroclinic interactions are to extreme rainfall associated with LTCs in China.

5.1. Typhoon Utor (2013)

Typhoon Utor (2013) is one of the strongest TCs over the western North Pacific in 2013. It made landfall in Yangjiang, Guangdong Province, China, on 14 August and persisted for about 4 days inland over South China and brought extensive precipitation to most regions of South China.

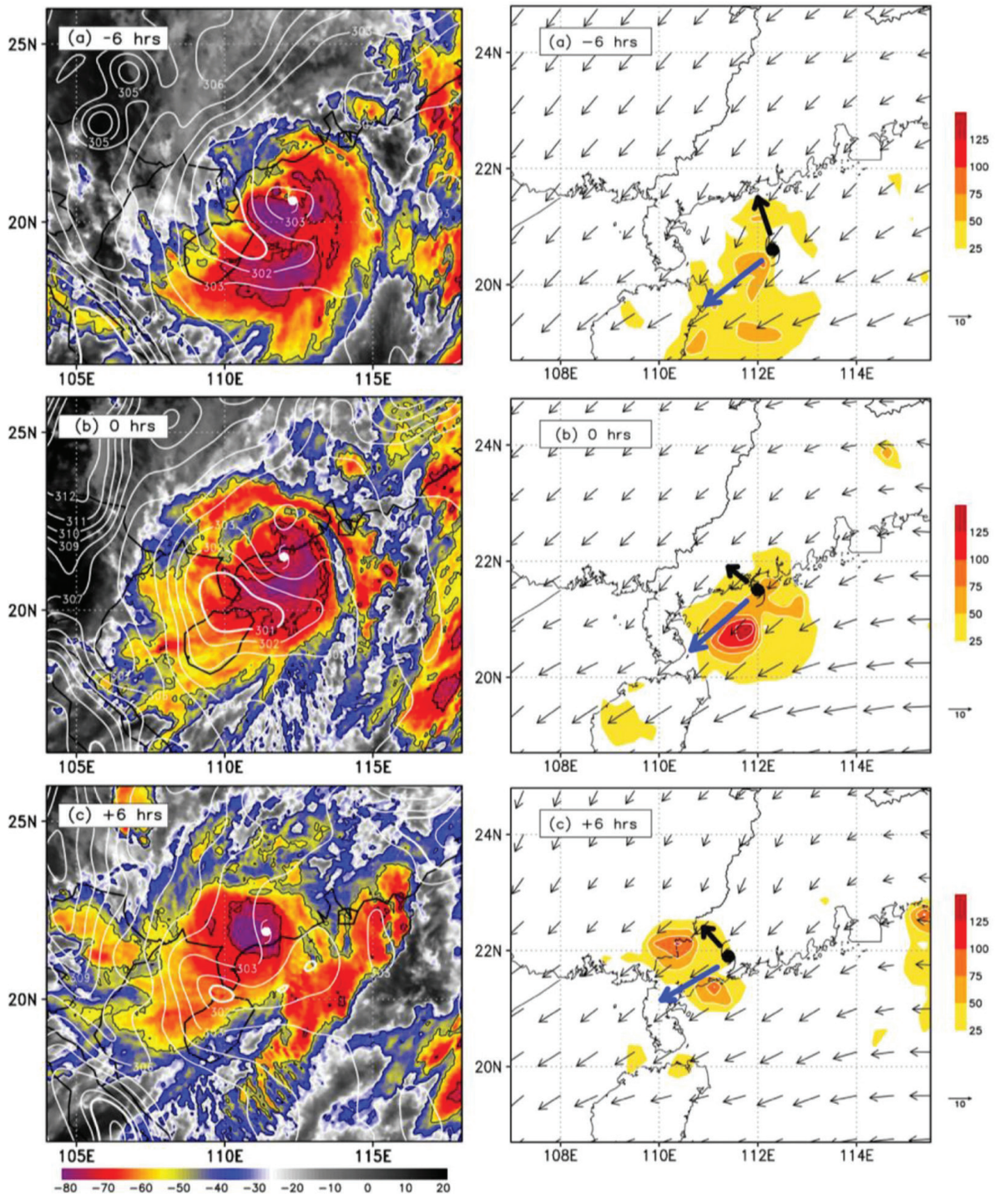

Figure 18. (Left) Potential temperature at 925 hPa (white contours with 1 K interval) and MTSAT IR cloud images (shading, K) at (a) 0000 UTC, (b) 0600 UTC, and (c) 1200 UTC 14 August 2013. The solid thick white contour of 301 K is used to denote the cold pool mentioned in the text. The TC center at the given time is marked by the typhoon symbol in each panel. (Right) Distributions of the environmental VWS vectors (m s^{-1}) and TRMM-3B42 6-h rainfall (mm) during the landfall of typhoon Utor in the first rainfall episode at (a) 6-h prior to landfall at 0000 UTC 14, (b) at the time of landfall at 0600 UTC 14, and (c) 6-h after landfall at 1200 UTC 14 August. Thick black vector denotes the moving direction of Typhoon Utor in the following 6 h in each panel. Blue arrows denote the averaged environmental VWS vector.

The rainfall distribution associated with Utor during landfall presented unique features [46, 47]. Meng and Wang [46, 47] used the ERA-Interim (European Centre for Medium-Range Weather Forecasting Interim reanalysis) data and the hourly surface rainfall observations to investigate the physical processes leading to large rainfall asymmetric distribution of Utor during its landfall. They found that the rainfall asymmetry was initially triggered by the effect of the environmental VWS, but enhanced by the cold pool dynamics which was triggered by the inland northwest dry air intrusion into Utor (**Figure 18a**). This cold pool enhancement process was understood based on the frontogenesis and quasi-balanced and ageostrophic Q-vector diagnosis (**Figure 18b**).

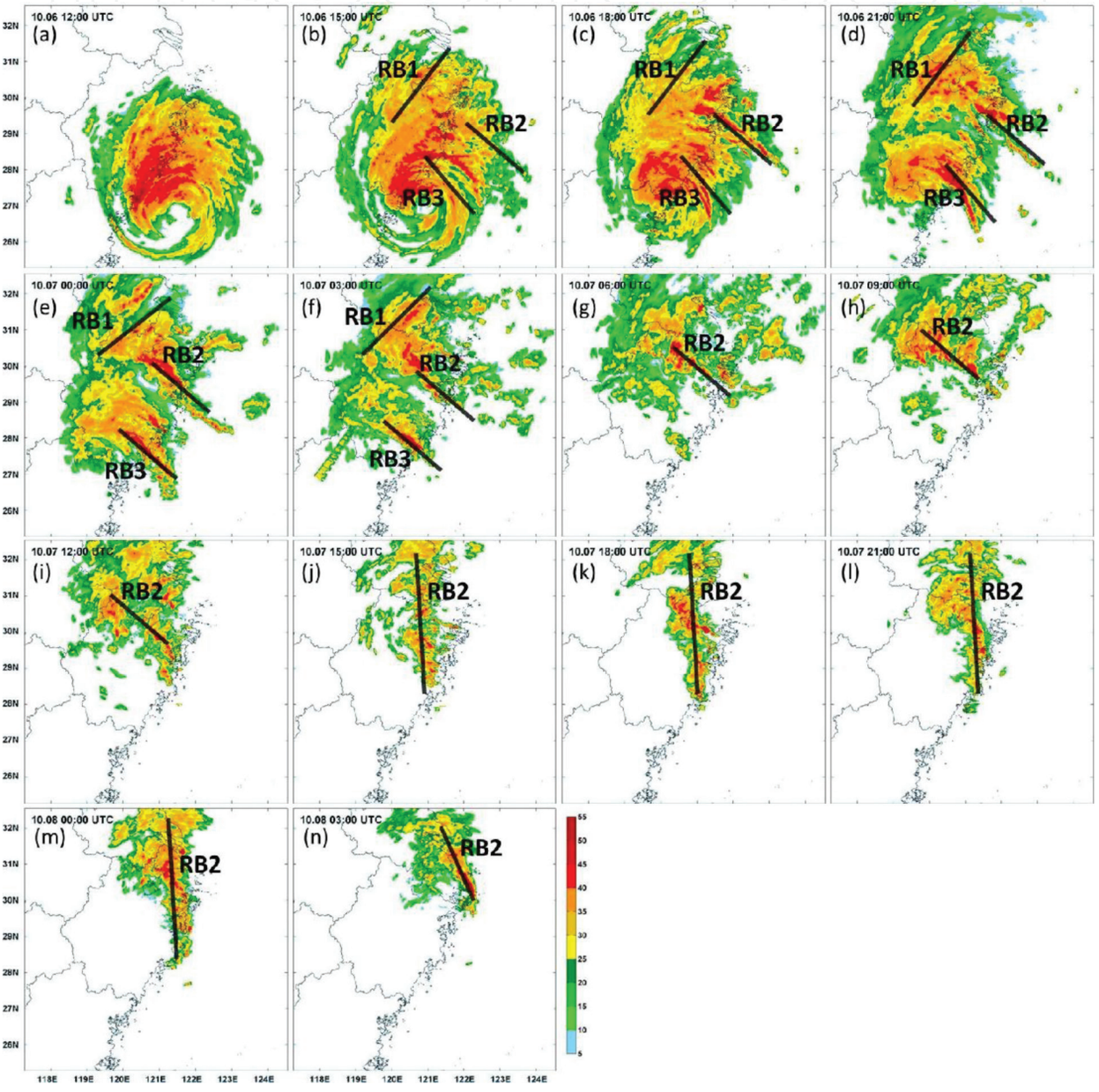

Figure 19. Observed composite radar reflectivity every 3 h from (a) 1200 UTC 6 Oct to (n) 0300 UTC 8 Oct 2013. RBs 1, 2, and 3 indicate rainbands associated with heavy rain. The locations of the four radar stations (Wenzhou, WZ; Ningbo, NB; Hangzhou, HZ; and Shanghai, SH) are shown in (a).

5.2. Typhoon Fitow (2013)

Typhoon Fitow (2013) is the strongest typhoon that made landfall over China in October since 1949. It caused severe damages in Zhejiang province due to its strong winds and heavy rainfall, with the minimum central sea-level pressure of 955 hPa and the maximum sustained 10-m wind speed of 42 m s^{-1} at landfall. The maximum gust wind speed of 76.1 m s^{-1} was observed at Shipingshan station (in the southeast coast of Zhejiang Province), which set a new record for LTCs over China. Fitow brought the strongest large-area 24-h precipitation in Zhejiang Province (100,000 km^2) as large as 137.5 mm on 07 October 2013. Consequently, Fitow resulted in severe urban water logging, flooding, debris flow disasters, and thus a direct economic loss of about 4.5 billion US dollars in Zhejiang Province. It also brought more than 1000 mm rainfall near Shanghai area in China, which was found to be related the cold air intrusion from northwest inland as shown in Bao et al. [67]. As shown in **Figure 19**, the rainfall systems included two parts: one was an outward-spiraling rainband, and the other was a frontal cloud system caused by coastal frontogenesis. Fitow was affected by a cold dry air intrusion from the north after landfall, which limited the rainfall in its inner core. However, an extended eastern warm moist air met the cold air from the north, leading to frontogenesis and heavy rainfall near Shanghai.

6. Discussions and remaining issues

Yu et al. [68] have presented verification of objective 0–6, 0–24, 24–48, 48–72, and 0–72 h rainfall forecasts for 25 LTCs and 133 operational numerical predictions from the tropical cyclone version of the Australian Community Climate and Earth System Simulator (ACCESS-TC). The contiguous rain area (CRA) method was used to diagnose the origin of systematic errors via adjustment of the forecast rain field by displacement, rotation, volume, and pattern. Mean track and intensity errors at 48 h for the sample are, respectively, 180 km and 10 knots. These represent a quite skillful level of performance of the ACCESS-TC. The mean values of equitable threat score, probability of detection, and false alarm ratio for the 30-mm isohyet for the unadjusted forecasts at 0–6 h are (0.22, 0.56, 0.66) (**Figure 20**). Unsurprisingly skill of the 24-h accumulated rainfall forecasts is the highest (0.36, 0.63, 0.40) for the 0–24-h forecast and then declines to (0.20, 0.42, 0.60) for the 72-h forecasts. Forecast skill also declines with rainfall amount.

With the use of the CRA method, skills show an improvement by about 15%, which are mostly associated with rainfall patterns, followed by displacement errors, particularly for very heavy rainfall. This suggests that rainfall prediction will continue to be improved with improving track prediction. However, further analysis showed that though the TC track and intensity is well forecasted, the rain distribution and structure is still a big challenge to the current numerical models, especially for the extremely heavy rainfall (>250 mm day^{-1}). It indicates that more work is needed to improve the initialization and prediction of TC structure. In particular, the TC size is a very important factor that could considerably affect the rainfall distribution in LTCs. However, this has not been studied so far mainly because the TC size information in the current TC best-track data is very limited for LTCs. In future studies, the

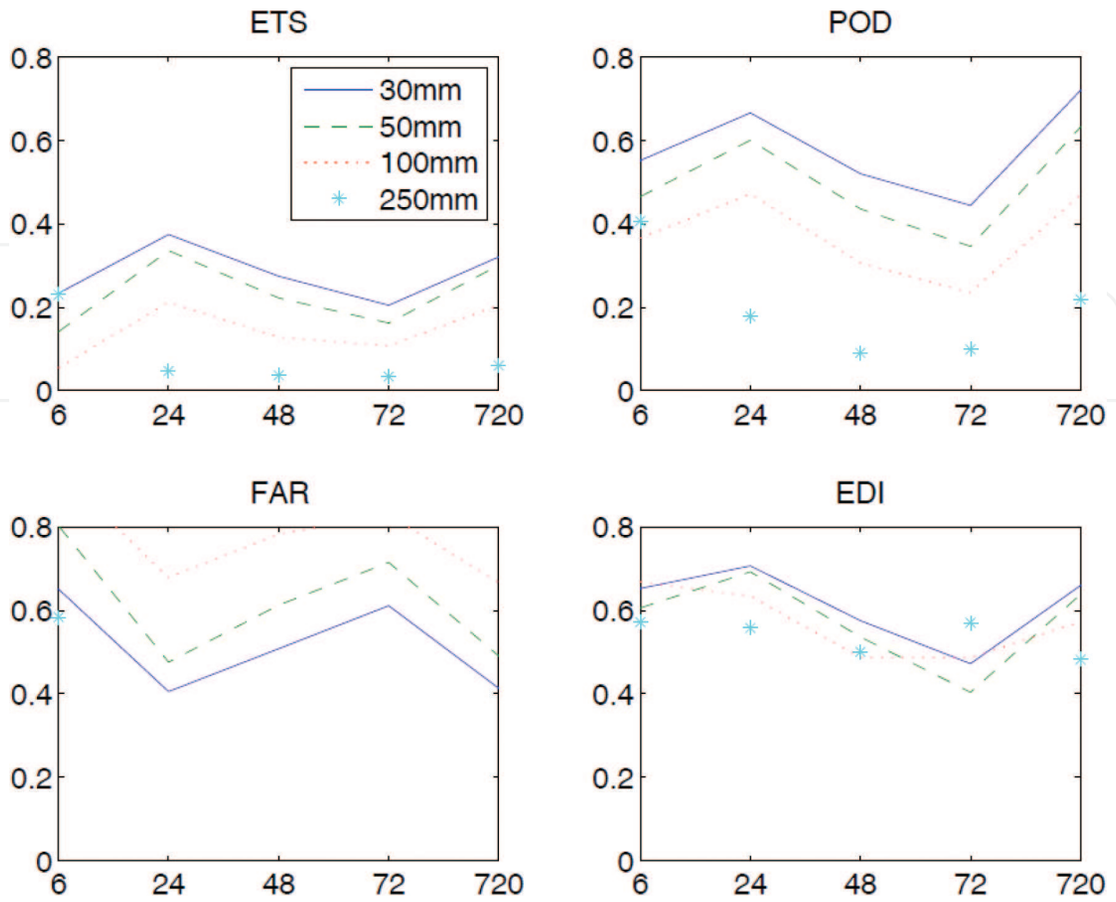

Figure 20. Conventional verification results of ETS, POD, FAR, and EDI for 30, 50, 100, and 250 mm rainfall thresholds. X-axis shows the accumulated rain forecast lead time of 0–6, 0–24, 24–48, 48–72, and 0–72 h, respectively. Y-axis shows the skill scores of the forecasts.

geostationary imagery or other data could be used to estimate the TC size parameter so that the effect of TC size on rainfall distribution of LTCs could be examined.

In fact, except for the limited ability of numerical forecast models, the observational capability of rainfall in LTCs is not good enough. As introduced in Section 2, compared with the surface radar and gauge data, the satellite rainfall estimates have relatively better spatial and temporal coverages, and therefore, the satellite-retrieved rainfall datasets (such as TRMM 3B42) have been applied extensively in the studies of rainfall in LTCs. However, the satellite quantitative precipitation estimates for LTCs still need large improvements because of their existing limitations, e.g., they would underestimate the heavy rain rates and the maximum rain rates. Therefore, the composites of rainfall characteristics were often analyzed and the uncertainties were usually represented using the box-plot analysis method in previous studies in Yu et al. [25, 26]. Though this would not significantly affect the major conclusions drawn in those previous studies, we still need to be aware of the limitations of data used. Therefore, future studies are needed to verify previous findings when better rainfall datasets become available.

Most of previous studies have focused mainly on the overall effects of environmental VWS, TC intensity and motion, and coastlines on the LTCs rainfall distribution and provide some

basic background and preliminary understanding to the LTC rainfall. However, it has shown that TC intensity does not have a robust relationship with the extreme rain metrics (including the maximum values of rain rate, rain area and total rain, and even the maximum rainfall location). Weak TCs may even have the maximum rain rates larger than strong TCs after landfall. Therefore, many unresolved scientific questions still remain especially for the extreme rainfall process in LTCs. Further work needs to pay more attention on the extreme rainfall mechanisms in LTCs.

Furthermore, the rainfall processes in LTCs are often very complicated and thus involve the effects of many factors and multi-scale interactions. Most of our current results and understanding are based on dynamical mechanisms, such as the VWS, TC translation, coastline, etc. So far few studies have paid attention to other possible effects, such as the thermodynamic effects (e.g., land-sea surface temperature contrast, differential radiation effects over land and ocean, effect of urbanization, etc.), even the cloud microphysical processes, and the possible effects of aerosols. Therefore, most of our current understanding and explanations are incomplete. In this regard, studies on mechanisms responsible for the rainfall distribution and its changes need to be further enhanced in the future. Particularly, with the development of both new observing systems and advanced numerical weather prediction models, some important physical processes, such as the boundary layer process and cloud microphysics, could be investigated and understood more comprehensively in the near future.

7. Concluding remarks

In this chapter, presented is the rainfall distribution in LTCs over China, including the axisymmetric and asymmetric distributions and the main control parameters, such as TC intensity, environmental VWS, TC motion, and coastline. The amplitudes of the WN 0–4 rainfall components have different evolutions during landfall among different regions. The WN-0, namely the axisymmetric rainfall component, accounts for about 50% of the total rainfall in LTCs in most studied areas and often decreases significantly after landfall.

On average, the axisymmetric rainfall is closely related to the TC intensity. The stronger TCs have larger averaged rainfall rate, larger mean peak axisymmetric rainfall rate, larger averaged total rainfall, larger averaged rainfall area, larger ratio of the axisymmetric component relative to total rainfall, but lower amplitudes of the WN-1, WN-2, WN-3, and WN-4 rainfall components relative to the total rainfall. The evolution of rainfall distribution is closely related to the changes of TC intensity from 24 h prior to landfall to 24 h after landfall. In the different intensity change categories, the RD LTCs show the most rapid decrease in both the total rainfall and the axisymmetric rainfall component.

In contrast, the extreme values of LTC rainfall (including the maximum rain rate, the maximum rain area, and the maximum total rainfall) are not highly related to TC intensity. In fact, weak storms may produce a greater maximum rain rate rather than strong TCs. This may be due to the effects of many other factors, such as environmental VWS and strong interactions with other synoptic weather systems and/or topography. The maximum asymmetric rainfall

in LTCs is usually located downshear and to its left, but more cyclonically downwind in strong LTCs such as CAT456, likely due to the relatively weaker VWS and the larger azimuthal advection by the stronger cyclonic circulation. The cyclonic rotation of the location of the LTC rainfall maxima also exists from South China to East China (HN, GD, Taiwan, Fujian, and Zhejiang), namely from the largest rainfall in the southwest and south quadrants in HN, GD, TW, and FJ, to the southeast quadrant in ZJ prior to landfall, and from the southwest to the northeast quadrant in LTCs after landfall. This cyclonic rotation is found to be tightly related to a similar cyclonic rotation of environmental VWS vectors from South China to East China. The latter is determined by the large-scale circulations, including the western North Pacific monsoon trough, subtropical high, and the midlatitude westerly systems. This indicates that environmental VWS should be a useful predictor for the asymmetric rainfall distribution in LTCs. The effect of TC motion (including direction and speed) on the rainfall distribution in LTCs is secondary compared with the effect of environmental VWS. However, the land-sea contrast may predominantly control the asymmetric rainfall distribution in LTCs when the ambient VWS is weak, as illustrated in a schematic **Figure 21**. When the environmental VWS is weak (less than 5 m s^{-1}), the asymmetric rainfall maximum in the periphery of a LTC may shift from the downshear and offshore side (shown by the shaded area in **Figure 21a**) to the upshear and onshore side (shown by the shaded area in **Figure 21b**).

Note that most of the findings discussed in this chapter are based on the composite analyses of satellite-retrieved products, individual LTC may be considerably deviated from the composite because of other possible involved complex scale multiple interactions and the complicated effect of topography. Typhoons Utor (2013) and Fitow (2013) are shown as examples to illustrate how important some processes other than VWS are in shaping the rainfall distribution in LTCs. The latest study by Bell et al. [69] shows that the microphysics of precipitation also plays an important role in TC extreme events. The cloud microphysics can be strongly modulated by the flow over terrain, resulting in the changes of the dominant processes in upslope or downslope winds [70], as well as changes in precipitation efficiency [71]. Mesoscale terrain in the coastal region can affect the spatial distribution and duration of rainfall by deflecting the TC track [72].

Current studies have not been comprehensive yet in several topics related to rainfall distribution and evolution in LTCs. For example, the rainfall diurnal cycle in LTC has recently been revealed by Hu et al. [73], but more work is necessary to understand the involved physical

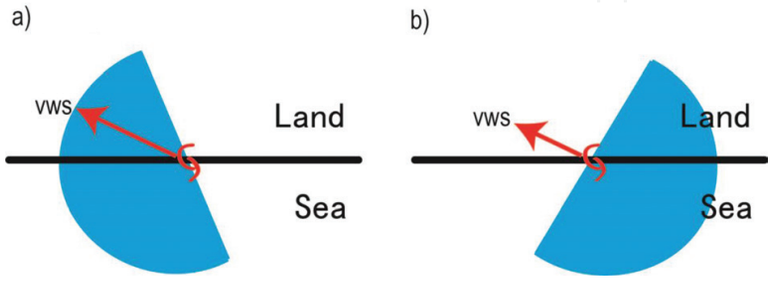

Figure 21. Schematic illustration of effects of both (a) strong and (b) weak environmental VWS (shown by the red arrows) combined with coastlines (shown by the bold black lines) on the rainfall asymmetries in LTCs.

mechanisms. The extreme rainfall in spiral rainbands is another topic not discussed/included here, so it needs to be thoroughly investigated because many extreme rainfall events in LTCs could be induced in spiral rainbands but not in the inner core region [74]. In addition, even a TC over the open ocean may also interact with neighboring weather systems, leading to rainfall in distant regions (over thousand kilometers from the TC), which is often called the TC remote effect [75]. These need to be comprehended further in future studies.

Finally, this chapter mainly summarizes the observational results and the related physical processes in determining both the axisymmetric and asymmetric distributions of rainfall in LTCs. Some recent efforts on improving the numerical prediction of TC-related rainfall have not been included. In fact, some recent studies have shown that radar data assimilation could substantially improve the extreme rainfall prediction skill, in particular for 0–24-h forecasts [76]. Nevertheless, this chapter provides a reference background for future studies on rainfall distribution in LTCs and for future efforts to improve rainfall forecast of LTCs not only in China but also in other regions of the world.

Acknowledgements

This work is supported in part by the National Basic Research and Development Project (973 program) of China under contract No. 2015CB452805 and in part by Key Program for International S&T Cooperation Projects of China (No. 2017YFE0107700).

Author details

Zifeng Yu[1] and Yuqing Wang[2,3]*

*Address all correspondence to: yuzf@typhoon.org.cn

1 Shanghai Typhoon Institute, China Meteorological Administration, Shanghai, China

2 State Key Laboratory of Severe Weather, Chinese Academy of Meteorological Sciences, China Administration, Beijing, China

3 Department of Atmospheric Sciences and International Pacific Research Center, University of Hawaii at Manoa, Honolulu, HI, USA

References

[1] Wang Y, Wu C-C. Current understanding of tropical cyclone structure and intensity changes – A review. Meteorology and Atmospheric Physics. 2004;**87**:257-278. DOI: 10.1007/s00703-003-0055-6

[2] Wang Y. Recent research progress on tropical cyclone structure and intensity. Tropical Cyclone Research and Review. 2012;**1**:254-275. DOI: 10.6057/2012TCRR02.05

[3] Marks Jr FD. Evolution of the structure of precipitation in Hurricane Allen (1980). Monthly Weather Review. 1985;**113**:909-930. DOI: 10.1175/1520-0493(1985)113<0909:EOTSOP>2.0.CO;2

[4] Merrill RT. Environmental influences on hurricane intensification. Journal of the Atmospheric Sciences. 1988;**45**:1678-1687. DOI: 10.1175/1520-0469(1988)045<1678:EIOHI>2.0.CO;2

[5] Jones SC. The evolution of vortices in vertical shear. I: Initially barotropic vortices. Quarterly Journal of the Royal Meteorological Society. 1995;**121**:821-851. DOI: 10.1002/qj.49712152406

[6] Jones SC. The evolution of vortices in vertical shear. II: Large-scale asymmetries. Quarterly Journal of the Royal Meteorological Society. 2000;**126**:3137-3160. DOI: 10.1002/qj.49712657008

[7] Jones SC. The evolution of vortices in vertical shear. III: Baroclinic vortices. Quarterly Journal of the Royal Meteorological Society. 2000;**126**:3161-3185. DOI: 10.1002/qj.49712657009

[8] Jones SC. On the ability of dry tropical-cyclone-like vortices to withstand vertical shear. Journal of the Atmospheric Sciences. 2004;**61**:114-119. DOI: 10.1175/1520-0469(2004)061<0114:OTAODT>2.0.CO;2

[9] Wang Y, Holland GJ. Tropical cyclone motion and evolution in vertical shear. Journal of the Atmospheric Sciences. 1996;**53**:3313-3332. DOI: 10.1175/1520-0469(1996)053<3313:TCMAEI>2.0.CO;2

[10] DeMaria M. The effect of vertical wind shear on tropical cyclone intensity change. Journal of the Atmospheric Sciences. 1996;**53**:2076-2088. DOI: 10.1175/1520-0469(1996)053<2076:TEOVSO>2.0.CO;2

[11] Frank WM, Ritchie EA. Effects of environmental flow upon tropical cyclone structure. Monthly Weather Review. 1999;**127**:2044-2061. DOI: 10.1175/1520-0493(1999)127<2044:EOEFUT>2.0.CO;2

[12] Frank WM, Ritchie EA. Effects of vertical wind shear on the intensity and structure of numerically simulated hurricanes. Monthly Weather Review. 2001;**129**:2249-2269. DOI: 10.1175/1520-0493(2001)129<2249:EOVWSO>2.0.CO;2

[13] Peng MS, Williams RT. Dynamics of vortex asymmetries and their influence on vortex motion on a β-plane. Journal of the Atmospheric Sciences. 1990;**47**:1987-2003. DOI: 10.1175/1520-0469(1990)047<1987:DOVAAT>2.0.CO;2

[14] Wang Y, Holland GJ. The beta drift of baroclinic vortices. Part I: Adiabatic vortices. Journal of the Atmospheric Sciences. 1996;**53**:411-427. DOI: 10.1175/1520-0469(1996)053<0411:TBDOBV>2.0.CO;2

[15] Wang Y, Holland GJ. The beta drift of baroclinic vortices. Part II: Diabatic vortices. Journal of the Atmospheric Sciences. 1996;**53**:3737-3756. DOI: 10.1175/1520-0469(1996)053<3737:TBDOBV>2.0.CO;2

[16] Bender MA. The effect of relative flow on the asymmetric structure in the interior of hurricanes. Journal of the Atmospheric Sciences. 1997;**54**:703-724. DOI: 10.1175/1520-0469(1997)054<0703:TEORFO>2.0.CO;2

[17] Peng MS, Jeng B-F, Williams RT. A numerical study on tropical cyclone intensification. Part I: Beta effect and mean flow effect. Journal of the Atmospheric Sciences. 1999;**56**:1404-1423. DOI: 10.1175/1520-0469(1999)056<1404:ANSOTC>2.0.CO;2

[18] Shapiro LJ. The asymmetric boundary layer flow under a translating hurricane. Journal of the Atmospheric Sciences. 1983;**40**:1984-1998. DOI: 10.1175/1520-0469(1983)040<1984:TABLFU>2.0.CO;2

[19] Dunion JP, Velden CS. The impact of the Saharan air layer on Atlantic tropical cyclone activity. Bulletin of the American Meteorological Society. 2004;**85**:353-365. DOI: 10.1175/BAMS-85-3-353

[20] Chen Y-S, Yau MY. Spiral bands in a simulated hurricane. Part I: Vortex Rossby wave verification. Journal of the Atmospheric Sciences. 2001;**58**:2128-2145. DOI: 10.1175/1520-0469(2001)058<2128:SBIASH>2.0.CO;2

[21] Wang Y. Vortex Rossby waves in a numerically simulated tropical cyclone. Part I: Overall structure, potential vorticity, and kinetic energy budgets. Journal of the Atmospheric Sciences. 2002;**59**:1213-1238. DOI: 10.1175/1520-0469(2002)059<1213:VRWIAN>2.0.CO;2

[22] Wang Y. Vortex Rossby waves in a numerically simulated tropical cyclone. Part II: The role in tropical cyclone structure and intensity changes. Journal of the Atmospheric Sciences. 2002;**59**:1213-1238. DOI: 10.1175/1520-0469(2002)059<1239:VRWIAN>2.0.CO;2

[23] Lonfat M, Marks Jr FD, Chen SS. Precipitation distribution in tropical cyclones using the tropical rainfall measuring mission (TRMM) microwave imager: A global perspective. Monthly Weather Review. 2004;**132**:1645-1660. DOI: 10.1175/1520-0493(2004)132<1645:PDITCU>2.0.CO;2

[24] Chen S, Knaff JA, Marks FD. Effects of vertical wind shear and storm motion on tropical cyclone rainfall asymmetries deduced from TRMM. Monthly Weather Review. 2006;**134**:3190-3208. DOI: 10.1175/MWR3245.1

[25] Yu Z, Wang Y, Xu H. Observed rainfall asymmetry in tropical cyclones making landfall over China. Journal of Applied Meteorology and Climatology. 2015;**54**:117-136. DOI: 10.1175/JAMC-D-13-0359.1

[26] Yu Z, Wang Y, Xu H, Davidson NE, Chen Y, Chen Y, Yu H. On the relationship between intensity and rainfall distribution in tropical cyclones making landfall over China. Journal of Applied Meteorology and Climatology. 2017;**56**:2883-2901. DOI: 10.1175/JAMC-D-16-0334.1

[27] Rogers R, Chen SS, Tenerelli J, Willoughby H. A numerical study of the impact of vertical shear on the distribution of rainfall in Hurricane Bonnie (1998). Monthly Weather Review. 2003;**131**:1577-1599. DOI: 10.1175//2546.1

[28] Lonfat M, Rogers R, Marchok T, Marks FD Jr. A parametric model for predicting hurricane rainfall. Monthly Weather Review. 2007;**135**:3086-3097. DOI: 10.1175/MWR3433.1

[29] Ueno M. Observational analysis and numerical evaluation of the effects of vertical wind shear on the rainfall asymmetry in the typhoon inner-core region. Journal of the Meteorological Society of Japan. 2007;**85**:115-136. DOI: 10.2151/jmsj.85.115

[30] Wingo MT, Cecil DJ. Effects of vertical wind shear on tropical cyclone precipitation. Monthly Weather Review. 2010;**138**:645-662. DOI: 10.1175/2009MWR2921.1

[31] Hence DA, Houze RA. Vertical structure of hurricane eyewalls as seen by the TRMM precipitation radar. Journal of the Atmospheric Sciences. 2011;**68**:1637-1652. DOI: 10.1175/2011JAS3578.1

[32] Reasor PD, Rogers R, Lorsolo S. Environmental flow impacts on tropical cyclone structure diagnosed from airborne Doppler radar composites. Monthly Weather Review. 2013;**141**:2949-2969. DOI: 10.1175/MWR-D-12-00334.1

[33] Tuleya RE, Kurihara Y. A numerical simulation of the landfall of tropical cyclones. Journal of the Atmospheric Sciences. 1978;**35**:242-257

[34] Tuleya RE, Bender MA, Kurihara Y. A simulation study of the landfall of tropical cyclones. Monthly Weather Review. 1984;**112**:124-136. DOI: 10.1175/1520-0493(1984)112<0124:ASSOTL>2.0.CO;2

[35] Jones RW. A simulation of hurricane landfall with a numerical model featuring latent heating by the resolvable scales. Monthly Weather Review. 1987;**115**:2279-2297. DOI: 10.1175/1520-0493(1987)115<2279:ASOHLW>2.0.CO;2

[36] Kepert JD, Wang Y. The dynamics of boundary layer jets within the tropical cyclone core. Part II: Nonlinear enhancement. Journal of the Atmospheric Sciences. 2001;**58**:2485-2501. DOI: 10.1175/1520-0469(2001)058<2485:TDOBLJ>2.0.CO;2

[37] Chan JCL, Liu KS, Ching SE, Lai EST. Asymmetric distribution of convection associated with tropical cyclones making landfall along the South China coast. Monthly Weather Review. 2004;**132**:2410-2420. DOI: 10.1175/1520-0493(2004)132<2410:ADOCAW>2.0.CO;2

[38] Kimball SK. Structure and evolution of rainfall in numerically simulated landfalling hurricanes. Monthly Weather Review. 2008;**136**:3822-3847. DOI: 10.1175/2008MWR2304.1

[39] Ramsay HA, Leslie LM, Kepert JD. A high-resolution simulation of asymmetries in severe southern hemisphere tropical cyclone Larry (2006). Monthly Weather Review. 2009;**137**:4171-4187. DOI: 10.1175/2009MWR2744.1

[40] Yu Z, Yu H, Gao S. Terrain impact on the precipitation of landfalling Typhoon Talim. Journal of Tropical Meteorology. 2010a;**16**:115-124. DOI: 10.3969/j.issn.1006-8775.2010.02.003

[41] Yu Z, Liang X, Yu H, Chan JCL. Mesoscale vortex generation and merging process: A case study associated with a post-landfall tropical depression. Advances in Atmospheric Sciences. 2010;**27**:356-370. DOI: 10.1007/s00376-009-8091-x

[42] Yu Z, Yu H. Application of generalized convective vorticity vector in a rainfall process caused by a landfalling tropical depression. Journal of Tropical Meteorology. 2012;**18**: 422-435

[43] Li Y, Cheung KKW, Chan JCL. Numerical study on the development of asymmetric convection and vertical wind shear during tropical cyclone landfall. Quarterly Journal of the Royal Meteorological Society. 2013;**140**:1866-1877. DOI: 10.1002/qj.2259

[44] Li Y, Cheung KKW, Chan JCL. Modelling the effects of land–sea contrast on tropical cyclone precipitation under environmental vertical wind shear. Quarterly Journal of the Royal Meteorological Society. 2014;**141**:396-412. DOI: 10.1002/qj.2359

[45] Xu W, Jiang H, Kang X. Rainfall asymmetries of tropical cyclones prior to, during, and after making landfall in South China and Southeast United States. Atmospheric Research. 2014;**139**:18-26. DOI: 10.1016/j.atmosres.2013.12.015

[46] Meng W, Wang Y. A diagnostic study on heavy rainfall induced by Typhoon Utor (2013) in South China: 1. Rainfall asymmetry at landfall. Journal of Geophysical Research-Atmospheres. 2016;**121**:12781-12802. DOI: 10.1002/2015JD024646

[47] Meng W, Wang Y. A diagnostic study on heavy rainfall induced by Typhoon Utor (2013) in South China: 2. Postlandfall rainfall. Journal of Geophysical Research-Atmospheres. 2016;**121**:12803-12819. DOI: 10.1002/2015JD024647

[48] Kepert JD. Observed boundary layer wind structure and balance in the hurricane core. Part I: Hurricane Georges. Journal of the Atmospheric Sciences. 2006;**63**:2169-2193.DOI: 10.1175/JAS3745.1

[49] Kepert JD. Observed boundary layer wind structure and balance in the hurricane core. Part II: Hurricane Mitch. Journal of the Atmospheric Sciences. 2006;**63**:2194-2211. DOI: 10.1175/JAS3746.1

[50] Chan JCL, Liang X. Convective asymmetries associated with tropical cyclone landfall. Part I: F-plane simulations. Journal of the Atmospheric Sciences. 2003;**60**:1560-1567. DOI: 10.1175/1520-0469(2003)60<1560:CAAWTC>2.0.CO;2

[51] Wong MLM, Chan JCL. Tropical cyclone motion in response to land surface friction. Journal of the Atmospheric Sciences. 2006;**63**:1324-1337. DOI: 10.1175/JAS3683.1

[52] Wong MLM, Chan JCL. Modeling the effects of land–sea roughness contrast on tropical cyclone winds. Journal of the Atmospheric Sciences. 2007;**64**:3249-3264. DOI: 10.1175/JAS4027.1

[53] Harnos SD, Nesbitt SW. Convective structure in rapidly intensifying tropical cyclones as depicted by passive microwave measurements. Geophysical Research Letters. 2011; **38**:L07805. DOI: 10.1029/2011GL047010

[54] Kieper EM, Jiang H. Predicting tropical cyclone rapid intensification using the 37 GHz ring pattern identified from passive microwave measurements. Geophysical Research Letters. 2012;**39**:L13804. DOI: 10.1029/2012GL052115

[55] Jiang H, Ramirez EM. Necessary conditions for tropical cyclone rapid intensification as derived from 11 years of TRMM data. Journal of Climate. 2013;**26**:6459-6470. DOI: 10.1175/JCLI-D-12-00432.1

[56] Alvey III GR, Zawislak J, Zipser E. Precipitation properties observed during tropical cyclone intensity change. Monthly Weather Review. 2015;**143**:4476-4492. DOI: 10.1175/MWR-D-15-0065.1

[57] Harnos SD, Nesbitt SW. Varied pathways for simulated tropical cyclone rapid intensification. Part I: Precipitation and environment. Quarterly Journal of the Royal Meteorological Society. 2016;**142**:1816-1831. DOI: 10.1002/qj.2780

[58] Jiang H, Halverson JB, Simpson J. On the differences in storm rainfall from hurricanes Isidore and Lili. Part I: Satellite observations and rain potential. Weather and Forecasting. 2008;**23**:29-43. DOI: 10.1175/2007WAF2005096.1

[59] Jiang H, Halverson JB, Zipser EJ. Influence of environmental moisture on TRMM-derived tropical cyclone precipitation over land and ocean. Geophysical Research Letters. 2008;**35**:L17806. DOI: 10.1029/2008GL034658

[60] Yu Z, Yu H, Chen P, Qian C, Yue C. Verification of tropical cyclone-related satellite precipitation estimates in Mainland China. Journal of Applied Meteorology and Climatology. 2009;**48**:2227-2241. DOI: 10.1175/2009JAMC2143.1

[61] Chen Y, Ebert EE, Walsh KJE, Davidson NE. Evaluation of TRMM 3B42 precipitation estimates of tropical cyclone rainfall using PACRAIN data. Journal of Geophysical Research – Atmospheres. 2013;**118**:1-13. DOI: 10.1002/jgrd.50250

[62] Chen Y, Ebert EE, Walsh KJE, Davidson NE. Evaluation of TMPA 3B42 daily precipitation estimates of tropical cyclone rainfall over Australia. Journal of Geophysical Research – Atmospheres. 2013;**118**:1-13. DOI: 10.1002/2013JD020319

[63] Kalnay E, et al. The NCEP/NCAR 40-year reanalysis project. Bulletin of the American Meteorological Society. 1996;**77**:437-471. DOI: 10.1175/1520-0477(1996)077<0437:TNYRP>2.0.CO;2

[64] Shu S, Ming J, Chi P. Large-scale characteristics and probability of rapidly intensifying tropical cyclones in the Western North Pacific Basin. Weather and Forecasting. 2012;**27**:411-423. DOI: 10.1175/WAF-D-11-00042.1

[65] Boyd JP. Chebyshev and Fourier Spectral Methods. 2nd ed. New York: Dover; 2001. 44 p

[66] Chen Y-S, Yau M Y. Asymmetric structures in a simulated landfalling hurricane. Journal of the Atmospheric Sciences. 2003;**60**:2294-2312. DOI: /10.1175/1520-0469(2003)060<2294:ASIASL>2.0.CO;2

[67] Bao X, Davidson NE, Yu H, Hankinson M, Sun Z, Rikus LJ, Liu J, Yu Z, Wu D. Diagnostics for an extreme rain event near Shanghai, during the landfall of Typhoon Fitow (2013). Monthly Weather Review. 2015;**143**:3377-3405. DOI: 10.1175/MWR-D-14-00241.1

[68] Yu Z, Chen Y, Ebert B, Davidson N E, Xiao Y, Yu H, Duan Y. Benchmark rainfall verification of ACCESS-TC operational landfall forecasts over China. Meteorological Applications. 2018 (submitted)

[69] Bell MM, Kingsmill DE, White AB. The ice water paths of small and large ice species in Hurricanes Arthur (2014) and Irene (2011). Journal of Applied Meteorology and Climatology. 2017;**56**:1383-1404. DOI: 10.1175/JAMC-D-16-0300.1

[70] DeHart JC, Houze RA. Orographic modification of precipitation processes in Hurricane Karl (2010). Monthly Weather Review. 2017;**145**:4171-4186. DOI: 10.1175/MWR-D-17-0014.1

[71] Huang H-L, Yang M-J, Sui C-H. Water budget and precipitation efficiency of Typhoon Morakot (2009). Journal of the Atmospheric Sciences. 2014;**71**:112-129. DOI: 10.1175/JAS-D-13-053.1

[72] Lin YL, Chen SH, Liu L. Orographic influence on basic flow and cyclone circulation and their impacts on track deflection of an idealized tropical cyclone. Journal of the Atmospheric Sciences. 2016;**73**:3951-3974. DOI: 10.1175/JAS-D-15-0252.1

[73] Hu H, Duan Y, Wang Y, Zhang X. Diurnal cycle of rainfall associated with landfalling tropical cyclones in China from rain-gauge observations. Journal of Applied Meteorology and Climatology. 2017;**56**:2595-2605. DOI: 10.1175/JAMC-D-16-0335.1

[74] Lin Y, Li Y, Li Q, Chen M, Xu F, Wang Y, Huang B. A long lasting vortex Rossby wave induced rainband of Typhoon Longwang (2005). Bulletin of the American Meteorological Society. 2018;**99** (in press). DOI: 10.1175/BAMS-D-17-0122.1

[75] Wang Y, Wang Y, Fudeyasu H. The role of Typhoon Songda (2004) in producing distantly located heavy rainfall in Japan. Monthly Weather Review. 2009;**137**:3699-3716. DOI: 10.1175/2009MWR2933.1

[76] Bao X, Wu D, Lei X, Ma L, Wang D, Zhao K, Jou BJ. Improving extreme rainfall forecast of Typhoon Morakot (2009) by assimilating radar data from Taiwan and mainland China. Journal of Meteorological Research. 2017;**31**:747-766. DOI: 10.1007/s13351-017-6007-8